Physics of Fluids

RESEARCH ARTICLE | OCTOBER 31 2022

Heat transfer and behavior of the Reynolds stress in Mach 6 boundary layer transition induced by first-mode oblique waves

Peixu Guo (郭培旭) ; Fangcheng Shi (施方成) ; Zhenxun Gao (高振勋) ; Chongwen Jiang (蒋崇文) ; Chun-Hian Lee (李椿萱) ; Chihyung Wen (温志湧)

Physics of Fluids 34, 104116 (2022)
https://doi.org/10.1063/5.0119211

Physics of Fluids ARTICLE scitation.org/journal/phf

Heat transfer and behavior of the Reynolds stress in Mach 6 boundary layer transition induced by first-mode oblique waves

Cite as: Phys. Fluids **34**, 104116 (2022); doi: 10.1063/5.0119211
Submitted: 8 August 2022 · Accepted: 3 October 2022 ·
Published Online: 31 October 2022

Peixu Guo (郭培旭),[1,2,a)] Fangcheng Shi (施方成),[1,3] Zhenxun Gao (高振勋),[1,b)] Chongwen Jiang (蒋崇文),[1] Chun-Hian Lee (李椿萱),[1] and Chihyung Wen (温志湧)[2]

AFFILIATIONS

[1]National Laboratory for Computational Fluid Dynamics, School of Aeronautic Science and Engineering, Beihang University, Beijing 100191, China
[2]Department of Aeronautical and Aviation Engineering, The Hong Kong Polytechnic University, Kowloon, Hong Kong, China
[3]College of Mechanical and Vehicle Engineering, Hunan University, Changsha 410082, China

[a)]**Electronic mail**: buaaguopeixu@buaa.edu.cn
[b)]**Author to whom correspondence should be addressed**: gaozhenxun@buaa.edu.cn

ABSTRACT

This paper investigates a Mach 6 oblique breakdown via direct numerical simulation in conjunction with stability and quadrant analyses. Particular emphasis is placed on, first, the heat transfer and mean flow distortion in the near-wall and outer transitional boundary layer, and, second, the flow events that are responsible for the production of the Reynolds stress. The energy budget reveals that enhancement of viscous dissipation due to mean flow distortion dominates the heat transfer overshoot, while the dissipation due to fluctuations is lesser but not negligible. Downstream of the location of the peak mean heat flux, the wall temperature gradient (non-dimensionalized by the freestream temperature and local boundary layer thickness) varies little, owing to the occurrence of breakdown and the establishment of self-similarity. Renormalized by the boundary layer thickness, a new correlation of the Stanton number shows no overshoot or difference between the original overshoot region and the turbulent region, which indicates the possibility of similarity once breakdown has occurred. In the outer region, enhanced advective heat exchange strongly reshapes the mean temperature profile. Because of successive modal growth and nonlinear saturation, the contributions of the primary oblique mode, streak mode, and a superharmonic to the outer advective heat transfer are found to compete near the location of the peak heat flux. From the perspective of fluid motions, quadrant analysis highlights the evenly and broadly distributed joint probability density function (PDF) of the fluctuating velocities during transition, which results in overproduction of the Reynolds stress, while the PDF is concentrated around zero in the turbulent region. The flow event Q2 (ejection) overtakes Q4 (sweep) in the outer boundary layer of the transitional region, mainly owing to the primary mode, while the two events become attenuated and nearly achieve balance when transition is complete.

I. INTRODUCTION

High-speed boundary layer transition has attracted much attention owing to its theoretical and engineering significance. Transition has considerable effects on drag reduction, flight control, and thermal protection system (TPS) design of hypersonic vehicles. However, the mechanisms associated with transitional flows and heat transfer performance, particularly for hypersonic flows, are not yet fully understood. Deeper knowledge of these mechanisms would help, for instance, in guiding the design of TPS.

From a fundamental point of view, natural transition is mostly associated with instability when the Reynolds number exceeds some threshold. During the linearly unstable stage, multimodal characteristics arise owing to an inviscid mechanism in high-Mach-number flows.[1,2] Among the sequence of higher modes, the Mack second mode is of particular interest because of its relatively high growth rate predicted by linear stability theory (LST). Therefore, this second mode commonly receives more attention than the first mode in hypersonic flows. However, the first mode may be dominant when receptivity,[3] wavepacket instability,[4] or nonlinear interactions[5–7] are taken

into consideration. Specifically, first, pure LST lacks a physical treatment of the initial disturbance amplitude, although this can be dealt with by a theoretical approach that considers leading-edge receptivity[8] or localized receptivity.[9] In the flow past a blunt body, the initial amplitude maximum of the first-mode waveband has the potential to overtake that of the second mode when the receptivity across the bow shock wave,[10,11] the entropy layer,[12,13] or the surface roughness[14] is considered. Second, the first-mode instability has been reported to overcome the second-mode instability in the wavepacket propagating over a compression corner if the wall blowing–suction strip is placed near the leading edge.[4] Third, upstream of the eventual breakdown, mode–mode interaction can potentially restrain the second mode yet promote the low-frequency mode via energy transfer.[7] Finally, in terms of aerodynamic performance, first-mode oblique breakdown has been found to trigger skin friction and heat transfer overshoot in the transitional region faster than second-mode fundamental or oblique breakdown.[15] The above considerations provide the motivation for the present paper to focus on the transition induced by the first mode, particularly the oblique breakdown scenario.

Following the linear instability stage, nonlinear wave–wave interaction and parametric resonance contribute to complicated flow phenomena and various breakdown regimes. Major breakdown scenarios contain K-type (fundamental), N-type (subharmonic), O-type (oblique), and detuned resonances initiated by the primary first mode or higher Mack modes.[16] Breakdown in real situations may be a complex mixture of these different types, and in numerical studies, this may be handled by the use of a wave packet pulse.[17] However, most previous numerical studies[15,18–23] have simply concentrated on the individual scenarios. The main purpose of these studies has been to shed light on the underlying mechanism in each scenario.

With its capability of resolving full flow scales, direct numerical simulation (DNS) is deemed to be an effective tool to investigate the breakdown mechanism. Early DNS work by Eißler and Bestek[18] demonstrated that a two-dimensional (2D) disturbance with a moderate amplitude tends to induce fundamental breakdown with the existence of three-dimensional (3D) disturbances, while subharmonic resonance occurs only if the secondary instability condition is fulfilled; that is, the phase velocities of 2D and 3D disturbances are synchronized. The growth rate of the disturbance in the fundamental breakdown is comparable to that in the subharmonic type, and thus, the dominant scenario is difficult to judge. Subsequent DNS work has contributed to understanding of first-mode subharmonic breakdown,[19,22] second-mode subharmonic breakdown,[21,23] and second-mode fundamental breakdown.[20,21,23]

Regarding the oblique breakdown scenario, this was confirmed by an early DNS study by Fasel *et al.*[24] to be a possible mechanism of turbulence generation. Pruett and Chang[25] examined second-mode oblique breakdown and found the pronounced fluctuation near the critical layer and the intense streamwise vorticity to be crucial factors before eventual breakdown. By imposing a 20-kHz initial disturbance, Mayer *et al.*[26] demonstrated good agreement between DNS and experimental data for the fluctuation amplitude and phase angle during Mach 2 boundary layer oblique breakdown. This work provided indirect experimental evidence for the oblique breakdown scenario. Later, Mayer *et al.*[27] concluded that the oblique breakdown may be dominant in a supersonic and quiet environment, because the disturbance amplitude threshold of oblique breakdown was found to be relatively low, while the significance of oblique breakdown for hypersonic cases was further confirmed by Franko and Lele[15] and Hartman *et al.*[28] The streak mode, actually the Fourier component (0, 2), was demonstrated by Mayer *et al.*[27] to be crucial in the oblique breakdown. This mode is generated by the nonlinear difference interaction of a pair of oblique waves with opposite wave angles[15] and essential transient growth.[29] Here, the Fourier component (m, n) denotes the harmonic with a frequency m times that of the primary instability wave and a spanwise/azimuthal wavenumber n times that of the primary instability wave. According to Fezer and Kloker,[30] oblique breakdown is dominant in a flat plate boundary layer, while fundamental breakdown is notable on a cone. A recent DNS study over a blunt cone at Mach 5.9 by Hartman *et al.*[28] showed that oblique waves, with a frequency of 250 kHz and azimuthal wavenumber of 50, could give rise to breakdown in the entropy layer upstream of the second-mode instability region. They also highlighted the importance of higher harmonics in addition to mode (0, 2) during breakdown. Because of the significance of oblique breakdown, other studies have also focused on appropriate control strategies in low-speed[31] and supersonic[32] flows by introducing additional streaks with a narrower spacing than mode (0, 2).

The transition process is accompanied by increases in surface skin friction C_f and heat flux q_w, which are to be expected since both momentum and energy transport are considerably enhanced during the strong instability and turbulent stages. However, nonmonotone variations of the mean C_f and q_w have frequently been observed in experimental studies, including, for example, flows over flat plates,[33] straight cones,[34] flared cones,[5,6] and the HIFiRE-1 forebody,[35] as well as in numerical studies.[15,20,36] Most commonly, one or two overshoot peaks may appear before C_f or q_w collapses onto the classical turbulent correlation. Franko and Lele[15] demonstrated that the most energetic mode (0, 2) in the considered Mach 6 oblique breakdown enhances vertical heat transfer and eventually results in heat transfer overshoot. In comparison, they found no obvious overshoot in the second-mode fundamental and oblique breakdown scenarios. Fasel *et al.*[20,21] showed that second-mode fundamental breakdown could generate at least double peaks in the surface heat flux in Mach 6 flow past sharp straight and flared cone models. The first peak, the subsequent valley, and the second peak of aerodynamic heating are relevant to the primary growth of mode (1, 0), the saturation of this mode, and the simultaneous rapid growth of higher harmonics, respectively. Furthermore, "primary" and "secondary" streaks were observed, along which the localized maximum Stanton number could reach three times the azimuthal-averaged value. By contrast, Lee's group[5–7] revealed another possibility that the temporary intermediate valley of heat transfer could be caused by nonlinear interaction of the second mode and the low-frequency mode. Dilatation-induced dissipation was also regarded as the major production term of the overshoot heat transfer in the second-mode initiated transition.

As shown in previous studies, particularly by Fasel *et al.*,[20,28] the contributions of higher harmonics to breakdown can definitely not be ignored. These modes, together with the primary one, are usually strongly competing and interacting in the late stage. Although the contributions of harmonics to aerodynamic heating are implicitly involved via modal growth, the relative contributions of each harmonic to the energy budget still appear to be unclear. Furthermore, the mean flow distortion (MFD) arising from nonlinear interactions has a significant influence in reshaping the mean flow profile and may play an

important role in the heat transfer overshoot. Examinations of the roles of superharmonics and MFD in heat transfer are necessary.

Another notable issue concerns the origin of the considerable production of turbulent kinetic energy (TKE) in the transitional region. As direct causes of TKE production, the overproduced Reynolds shear stress and wall-normal component of the Reynolds heat flux have been recognized as responsible for the overshoots of the time-averaged skin friction and heat flux.[15] From the perspective of fluid motion, the major contributions to the Reynolds shear stress can be decomposed into quadrants in terms of flow events via the well-established approach of Willmarth and Lu.[37] The majority of studies in this area have applied quadrant analysis to fully developed turbulence[38] rather than transitional flows. With regard to transitional flows, Volino and Simon[39] found that an incompressible transitional heated boundary layer is dominated by the hot ejection of large-scale eddies. Nolan *et al.*[40] presented a systematic quadrant analysis of particle image velocimetry (PIV) data from low-speed bypass transitional flows. The initial growth in TKE production was observed to be located in the outer region, actually at about 0.3 times the local boundary layer thickness. The event Q2 (ejection) was also regarded as the main source of TKE production in the bypass transition. Nolan and Zaki[41] further confirmed the significance of Q2 (ejection) at the boundary layer edge and Q4 (sweep) near the wall for bypass transition. Park *et al.*[42] concluded that there existed some similarities in significant flow structures and transport processes between turbulent spots and the fully developed turbulent region. However, to the best of our knowledge, neither the mechanism of the hypersonic oblique breakdown of the natural transition nor that of the heat transfer overshoot have been revealed by quadrant analysis. In the present paper, therefore, we focus on the mechanisms of Mach 6 oblique breakdown as well as the overshoot of skin friction and heat flux by utilizing DNS, parallel and nonparallel stability analyses, and quadrant analysis. We are also motivated by the comparative study by Mayer *et al.*[26] of DNS and experiment results for oblique breakdown initiated by a 20-kHz first-mode disturbance. In the present paper, the oblique breakdown is induced by a disturbance frequency of 23.88 kHz, which corresponds to the maximum first-mode growth rate near the blowing–suction strip. Thus, our DNS data enable us to explain the aerodynamic and aerothermal performance during the experimentally observed first-mode oblique breakdown with a frequency of tens of kilohertz.

The remainder of the paper is organized as follows. Section II describes the governing equations and numerical methods of the DNS and flow stability analyses. Descriptions of the computational model and case are also included. Section III presents an analysis of instantaneous, statistical and Fourier modal results. Section IV presents analyses of the internal energy budget and mean flow profiles and reveals the separate contributions of, for example, MFD and higher harmonics. Section V presents the quadrant analysis in critical regions. Section VI gives concluding remarks.

II. METHODOLOGY

A. Governing equations and numerical methods

1. Direct numerical simulation

The DNS is based on the 3D compressible Navier–Stokes (N–S) equations for a calorically perfect gas, which can be written in a Cartesian coordinate system as

$$\begin{cases} \dfrac{\partial \rho^*}{\partial t^*} + \dfrac{\partial}{\partial x_j^*}\left(\rho^* u_j^*\right) = 0, \\ \dfrac{\partial}{\partial t^*}\left(\rho^* u_i^*\right) + \dfrac{\partial}{\partial x_j^*}\left(\rho^* u_i^* u_j^* + \delta_{ij} p^*\right) = \dfrac{\partial \tau_{ij}^*}{\partial x_j^*}, \\ \dfrac{\partial}{\partial t^*}\left(\rho^* E^*\right) + \dfrac{\partial}{\partial x_j^*}\left[\left(\rho^* E^* + p^*\right) u_j^*\right] = \dfrac{\partial}{\partial x_j^*}\left(u_i^* \tau_{ij}^* - q_j^*\right). \end{cases} \tag{1}$$

Here, the asterisk denotes a dimensional variable, the subscripts i and j are indices in Einstein notation (with summation over repeated indices), δ_{ij} is the Kronecker delta function, and x_j are Cartesian coordinates. The variables t, u, ρ, p, and T are the time, velocity, density, pressure, and temperature, respectively, while the velocity vector has the equivalent forms $\mathbf{V} = (u_1, u_2, u_3) = (u, v, w)$. The quantities τ_{ij}, E, and q_j are the viscous stress tensor, the total energy per unit volume, and the heat flux vector in the x_j direction, which in dimensional form can be expressed as

$$\tau_{ij}^* = \mu^* \left(\frac{\partial u_i^*}{\partial x_j^*} + \frac{\partial u_j^*}{\partial x_i^*}\right) + \lambda^* \frac{\partial u_k^*}{\partial x_k^*} \delta_{ij}, \tag{2}$$

$$E^* = e^* + \frac{1}{2} u_i^* u_i^*, \quad q_j^* = -\kappa^* \frac{\partial T^*}{\partial x_j^*}. \tag{3}$$

Here, μ, λ, and κ are the dynamic viscosity, the second viscosity, and the thermal conductivity, respectively. The variable e represents the internal energy per unit volume, which is calculated as $e^* = c_v^* T^*$, where c_v is the specific heat at constant volume. For a perfect gas, c_v is given by $c_v^* = R^*/(\gamma - 1)$, where the gas constant $R^* = 287.053$ J/(kg K) for air and the specific heat ratio γ is set to 1.4. The dynamic viscosity is computed from Sutherland's law

$$\frac{\mu^*}{\mu_0^*} = \left(\frac{T^*}{T_0^*}\right)^{3/2} \frac{T_0^* + C_0^*}{T^* + C_0^*}, \tag{4}$$

where $\mu_0^* = 1.7894 \times 10^{-5}$ kg/(m s), $T_0^* = 288.15$ K, and $C_0^* = 110.4$ K. In the present paper, the second viscosity λ is assumed to satisfy Stokes' hypothesis and the thermal conductivity is determined by $\kappa^* = \mu^* c_p^*/Pr$, where the Prandtl number Pr is set to 0.72. To close the N–S equations, the equation of state for an ideal gas, $p^* = \rho^* R^* T^*$, is added.

Subsequently, the N–S equations can be expressed in conservative form as

$$\frac{\partial \mathbf{Q}}{\partial t^*} + \frac{\partial \mathbf{F}}{\partial x^*} + \frac{\partial \mathbf{G}}{\partial y^*} + \frac{\partial \mathbf{H}}{\partial z^*} = \frac{\partial \mathbf{F}_v}{\partial x^*} + \frac{\partial \mathbf{G}_v}{\partial y^*} + \frac{\partial \mathbf{H}_v}{\partial z^*}, \tag{5}$$

where $\mathbf{Q}$ denotes the conservative variables; $\mathbf{F}$, $\mathbf{G}$, and $\mathbf{H}$ are the inviscid flux vectors; and $\mathbf{F}_v$, $\mathbf{G}_v$, and $\mathbf{H}_v$ are the viscous flux vectors (for the detailed expressions, see Ref. 43). The non-dimensionalized N–S equations are then obtained via the following transformation while keeping the same written form:

$$\begin{gathered} t = \frac{t^*}{l_{\mathrm{ref}}/u_\infty^*}, \quad x_i = \frac{x_i^*}{l_{\mathrm{ref}}}, \quad u_i = \frac{u_i^*}{u_\infty^*}, \\ \rho = \frac{\rho^*}{\rho_\infty^*}, \quad p = \frac{p^*}{\rho_\infty^* u_\infty^{*2}}, \quad T = \frac{T^*}{T_\infty^*}, \\ \mu = \frac{\mu^*}{\mu_\infty^*}, \quad \kappa = \frac{\kappa^*}{\mu_\infty^* u_\infty^{*2}/T_\infty^*}, \quad e = \frac{e^*}{u_\infty^{*2}}, \quad R = \frac{R^*}{u_\infty^{*2}/T_\infty^*}, \end{gathered} \tag{6}$$

where l_{ref} is the reference length scale. Finally, the governing equation is transformed from the Cartesian to a generalized curvilinear coordinate system and solved by our in-house code called ACANS (Aerodynamic Combustion and Aerothermodynamic Numerical Simulation) based on the finite difference method.

In the numerical method, time marching is achieved by the three-stage third-order total variation diminishing (TVD) Runge–Kutta method, which enables time-accurate simulation. In the numerical scheme for inviscid terms, the seventh weighted essentially nonoscillatory (WENO) schemes are applied to ensure high-order resolution of the smooth flow field while maintaining robustness around possible shocklets or strong wavelets induced by wall blowing suction. The viscous terms are discretized by a second- or fourth-order central difference scheme. The statistical results are shown to be insensitive to the order of viscous term discretization under the considered mesh resolution, and thus, the second order is chosen for overall simulation. The Appendix presents a preliminary successful validation case for ACANS of the simulation of mode S propagating in a Mach 6 2D boundary layer.

2. Stability analysis

To compare with DNS results and identify the linear and nonlinear stages of transition, parallel and nonparallel linear stability analyses are conducted via our code called CHASES. With a given base flow, CHASES enables theoretical calculation of convective instability problems for compressible flows. Taking Cartesian coordinates for example, the instantaneous flow field is considered as the superposition of the steady base flow ϕ_b solved from the boundary layer equation and the disturbance ϕ',

$$\phi(x,y,z,t) = \phi_b(x,y,z) + \phi'(x,y,z,t), \tag{7}$$

where the disturbance is assumed to contain a rapidly varying wave function and a slowly varying shape function $\boldsymbol{\psi}$ in the parabolized stability equation (PSE) formulation[44]

$$\phi' = \boldsymbol{\psi}(x,y)\exp\left\{\mathrm{i}\left[\int_{x_0}^{x}\alpha(\bar{x})\,d\bar{x} + \beta z - \omega t\right]\right\} + \text{c.c.} \tag{8}$$

Here, α, β and ω are the streamwise wavenumber, spanwise wavenumber, and angular frequency, respectively; the initial coordinate x_0 denotes the distance from the inflow location to the leading edge, $\mathrm{i} = \sqrt{-1}$, and "c.c." denotes the complex conjugate. The shape function of the disturbance is written in vector form as $\boldsymbol{\psi} = (\hat{\rho}, \hat{u}, \hat{v}, \hat{w}, \hat{T})^{\mathrm{T}}$, where superscript "T" denotes the transpose.

Substituting Eqs. (7) and (8) into the N–S equations, applying the parabolized approximation, and dropping the nonlinear terms finally yield the following form of the governing equation for the nonparallel analysis:

$$(\mathscr{L}_0 + \mathscr{L}_1)\boldsymbol{\psi} + \mathscr{L}_2\frac{\partial\boldsymbol{\psi}}{\partial x} + \frac{d\alpha}{dx}\mathscr{L}_3\boldsymbol{\psi} = 0, \tag{9}$$

where $\mathscr{L}_0$, $\mathscr{L}_1$, $\mathscr{L}_2$, and $\mathscr{L}_3$ represent the operators arising from the effects of the locally parallel flow, nonparallel base flow, nonparallel shape function, and nonparallel wavenumber, respectively.[45] The boundary conditions for the shape function are unified as

$$\hat{u} = \hat{v} = \hat{w} = \hat{T} = 0, \quad y = 0 \quad \text{or} \quad y \to \infty, \tag{10}$$

TABLE I. Conditions for freestream, wall boundary, and inlet location parameters.

Ma_∞	T^*_∞ (K)	Re_{unit} (m^{-1})	T^*_w (K)	$T^*_w/T^*_{\text{adb},l}$	x^*_0 (m)
6	55	1×10^7	300	0.767	0.02

while the boundary density disturbance is solved from the wall-normal momentum equation. To close the problem, an iterative scheme for the wavenumber is adopted under the ansatz of a streamwise slowly varying shape function, which is given by

$$\alpha_{\text{new}} = \alpha_{\text{old}} - \mathrm{i}\frac{1}{E}\int_0^\infty \rho_b\left(\hat{u}^\dagger\frac{\partial\hat{u}}{\partial x} + \hat{v}^\dagger\frac{\partial\hat{v}}{\partial x} + \hat{w}^\dagger\frac{\partial\hat{w}}{\partial x}\right)dy, \tag{11}$$

where superscript † denotes the complex-conjugate quantity. If the nonparallel effect can be ignored, then the terms containing $\mathscr{L}_1 \sim \mathscr{L}_3$ in Eq. (9) can be removed, which corresponds to a switch from the PSE to an LST analysis.

With regard to the numerical techniques of the PSE analysis, the first-order Euler backward scheme is applied for streamwise marching, while the Chebyshev pseudospectral method is used for the wall-normal difference. The Vigneron technique is used to restrain the numerical instability originating from residual ellipticity.[46] In the LST analysis, Malik's[47] global algorithm using the Chebyshev pseudospectral method and a local algorithm with compact fourth-order difference are used for the wall-normal discretization. The LST eigenvalue problem is solved by the external Intel math kernel library (MKL). Iterative procedures ensure that both PSE and LST will give a converged complex wavenumber α with at least four valid digits. Several validation cases for LST have been presented in our previous papers,[48,49] while the case for PSE is shown in the Appendix.

B. Computational model and case description

We now describe the computational model and numerical case. The main computational condition is given in Table I, where subscripts ∞ and w denote the freestream and wall quantities, respectively. The unit Reynolds number is denoted by Re_{unit}. The adiabatic wall temperature $T^*_{\text{adb},l}$ for laminar flows equals $[1 + r(\gamma-1)Ma^2_\infty/2]T^*_\infty$, where the recovery factor $r = Pr^{1/2}$. As shown in Fig. 1, a Mach 6 transitional flat-plate boundary layer will be simulated and theoretically analyzed,

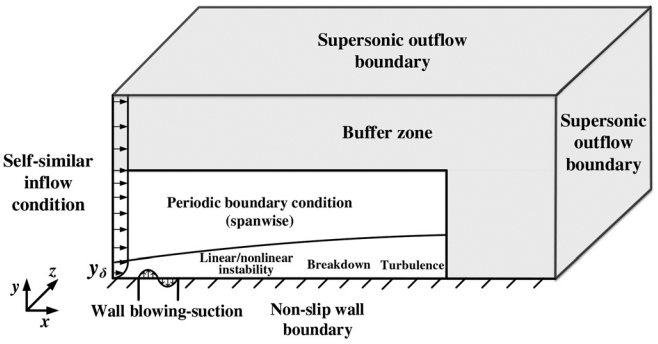

FIG. 1. Sketch of DNS strategies for the first-mode-induced flat-plate boundary layer transition.

where the x, y, and z Cartesian coordinates correspond to the streamwise, wall-normal, and spanwise directions, respectively. The steady base flow at the inflow boundary is specified as a profile extracted from the self-similar laminar solution, where the distance to the leading edge is given by x_0^* in Table I. To excite the downstream instability, temporally and spanwise periodic disturbances are artificially imposed on the wall-normal momentum of the solid wall, simulating a blowing–suction strip near the inlet. In this way, with the leading-edge receptivity being ignored, DNS will place special emphasis on the downstream linear and nonlinear instabilities as well as the breakdown. The mathematical form of the disturbance is given by[50,51]

$$(\rho v)'_w = A_w f(\xi)\cos(2\pi z/\lambda_z)\sin(2\pi f t). \tag{12}$$

Here

$$f(\xi) = 15.1875\xi^5 - 35.4375\xi^4 + 20.25\xi^3, \tag{13}$$

$$\xi = \begin{cases} (x^* - x_1^*)/(x_m^* - x_1^*), & x_1^* \le x^* \le x_m^*, \\ (x_2^* - x^*)/(x_2^* - x_m^*), & x_m^* < x^* \le x_2^*, \end{cases} \tag{14}$$

where the blowing suction occurs between $x_1^* = 0.033\,64$ m and $x_2^* = 0.045$ m, and $x_m^* = (x_1^* + x_2^*)/2$. The dimensionless amplitude parameter A_w is set to 0.02, which is moderate in magnitude. With this value of the amplitude parameter, the natural transition scenario is shown to occur within the expected computational domain. The frequency and spanwise wavenumber of the forcing are set to $f^* = 23.88$ kHz and $\lambda_z^* = 12.45$ mm, respectively. These two parameter values are decided by the first-mode neutral curve provided by LST, which ensures that the primary wave is locally unstable near the blowing–suction strip and that first-mode-induced oblique breakdown finally occurs. As mentioned in Sec. I, this setting of the frequency enables study of first-mode oblique breakdown with a frequency of tens of kilohertz, as has been observed in experiments.

Without the introduction of the two-dimensional primary mode, Eq. (12) is actually the sum of a pair of oblique waves with opposite wave angles, which may lead to oblique breakdown. In terms of the surface velocity condition, the wall boundary is given by the no-penetration condition except at the blowing–suction strip, while a no-slip condition is imposed on the whole solid wall. To minimize the reflection of disturbances on the outlet boundary, an extra sponge zone is added on the upper and outflow boundaries of Fig. 1, with an exponentially growing grid spacing and thus increasing numerical dissipation. A supersonic outflow condition implemented by extrapolation is given, while the higher-order effect of the limited subsonic region is neglected. A periodic boundary condition is used in the spanwise direction.

The mesh information is shown in Table II. Here, n_x, n_y, and n_z denote the node numbers in the x, y, and z directions, while L_x, L_y, and L_z are the respective lengths of the main computational domain. In addition to the baseline case for subsequent discussions, further comparative studies (unshown) have been performed to confirm the convergence of the grid size, domain size, and first-mesh wall-normal grid spacing. The time step of the Runge–Kutta method is given by $\Delta t^* = 1.5 \times 10^{-8}$ s. The dimensionless time step of the flow through the computational domain is given by $u_\infty^* \Delta t^*/L_x \approx 2 \times 10^{-5}$. Numerical tests confirm the convergence of the time step selection (not shown here). The structured mesh is orthogonal to reduce potential mesh-induced numerical error. The grid spacings are uniform in the streamwise and spanwise directions, while the mesh is stretched in the wall-normal direction. Here, in Table II, to calculate Δx^+, Δy^+, and Δz^+, the skin friction C_f that gives the wall friction velocity is estimated by the van Driest II formula based on Re_θ[15] at the location $x^* = 0.7$ m, which is subsequently found to be in the fully turbulent region.

TABLE II. Mesh information for DNS.

n_x	n_y	n_z	L_x(m)	L_y(m)	L_z(m)	Δx^+	$\Delta y^+_{\min}$	Δz^+
2301	123	176	0.7	0.15	0.035	5.91	0.39	3.94

Once the preceding computational setup has been prepared, DNS is performed on the Dawning 4000 L supercomputer of Beihang University. During the computation, a statistical analysis is carried out until the flow field is statistically stationary after over ten time units of flow through the computational domain. The instantaneous data are output every 30 steps and accumulate to give a total of about 7 TB. Finally, a temporal and spatial (spanwise) bi-Fourier transformation, implemented by the Intel MKL, is performed to obtain modal information. The sampling frequency of the Fourier analysis is two orders of magnitude larger than the primary wave frequency to ensure the accuracy of the higher harmonics. The total sampling period is sufficiently long that the minimal frequency of the Fourier analysis is one order of magnitude smaller than the primary wave frequency.

III. FLOW ANALYSIS

A. Instantaneous flow field

B. Statistical results

Figure 2 displays the instantaneous field of the streamwise velocity on the x–y and x–z planes. The contours clearly illustrate the complete development of the boundary layer from early instability to breakdown and full turbulence. In addition, the features of the breakdown are associated with the wall-normal height. The flow at $y^* = 2.5$ mm, close to the critical layer position at $x^* \approx 0.25$ m, transitions dramatically, as characterized by the formation and breakdown of staggered Λ-vortices. Here, the critical layer position of the profile corresponds to the height at which the base velocity equals the phase speed of the primary wave. By contrast, in the inner region at $y^* = 1$ mm ($y/y_\delta \approx 0.3$ at $x^* \approx 0.25$ m) in Fig. 2, evident breakdown of low-speed streaks can be identified. This observation seemingly agrees with the classical finding of Kline *et al.*[52] that turbulence is generated by bursting of near-wall low-speed streaks. The high-speed Λ-like structure in between may be linked with the staggered Λ-vortex in the upper layer inferred from the shape of the structure. The low-speed streaks are observed to have a spanwise spacing approximately half of the initial primary wave, that is, $\lambda_z^*/2 = 6.225$ mm. This indicates that the streak mode (0, 2) could be dominant in the near-wall region.

Figure 3 shows that the spanwise distortion of the streamwise velocity is minor at the profile $x^* = 0.1$ m, but gradually grows from the location $x^* = 0.15$ m to $x^* = 0.25$ m. With regard to the spanwise scale of the structure in this early stage, the dominant wave near the boundary layer edge has a wavelength close to the primary one, that is, $\lambda_z^* = 12.45$ mm. Toward the wall, the significant wavelength appears to be $\lambda_z^*/2$, which indicates the existence of a higher harmonic arising

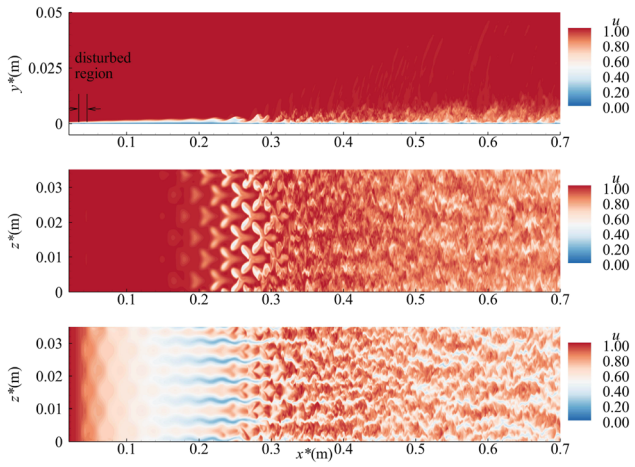

FIG. 2. Instantaneous field of streamwise velocity on the planes $z^* = L_z/2$ (top), $y^* = 2.5$ mm (middle), and $y^* = 1$ mm (bottom).

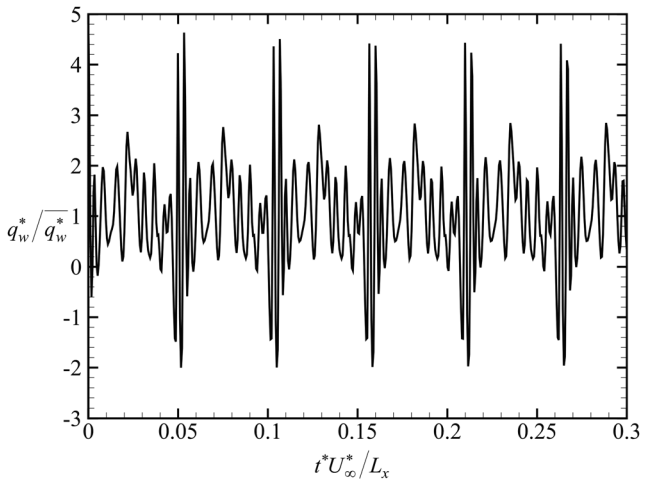

FIG. 4. Instantaneous heat flux non-dimensionalized by the time-averaged value varying with time on the symmetry plane at $x^* = 0.33$ m (show only per 30 time steps).

from secondary instability. Figures 3(c) and 3(d) show that the critical layer position of the primary wave turns out to be the height at which the velocity field is the most strongly distorted. This height in Fig. 3(d) seems to be near the crossing point of spanwise-distorted waves. Subsequently, in Fig. 3(e), breakdown occurs almost in the vicinity of that crossing point near the boundary layer edge. Thus, the critical layer instability is observed to be responsible for the final nonlinear breakdown. The primary mode (1, 1) near the critical layer and the near-wall modes $(m, 2)$ that have wavelength $\lambda_z^*/2$ are probably dominant in this stage.

The behavior of the instantaneous heat transfer is also of interest. Figure 4 shows the instantaneous surface heat flux at $x^* = 0.33$ m (the streamwise peak location of the mean heat flux), which is non-dimensionalized by the time-averaged value. Here, $\bar{\phi}$ denotes the time average of ϕ. It can be seen that the maximum instantaneous heat flux is around 4.6 times the average on the symmetry plane $z = 0$, while this ratio varies from 3.0 to 5.0 on various spanwise slices (not shown here). The intense temperature fluctuation also results in a negative instantaneous heat flux concentrated in the short-timescale history.

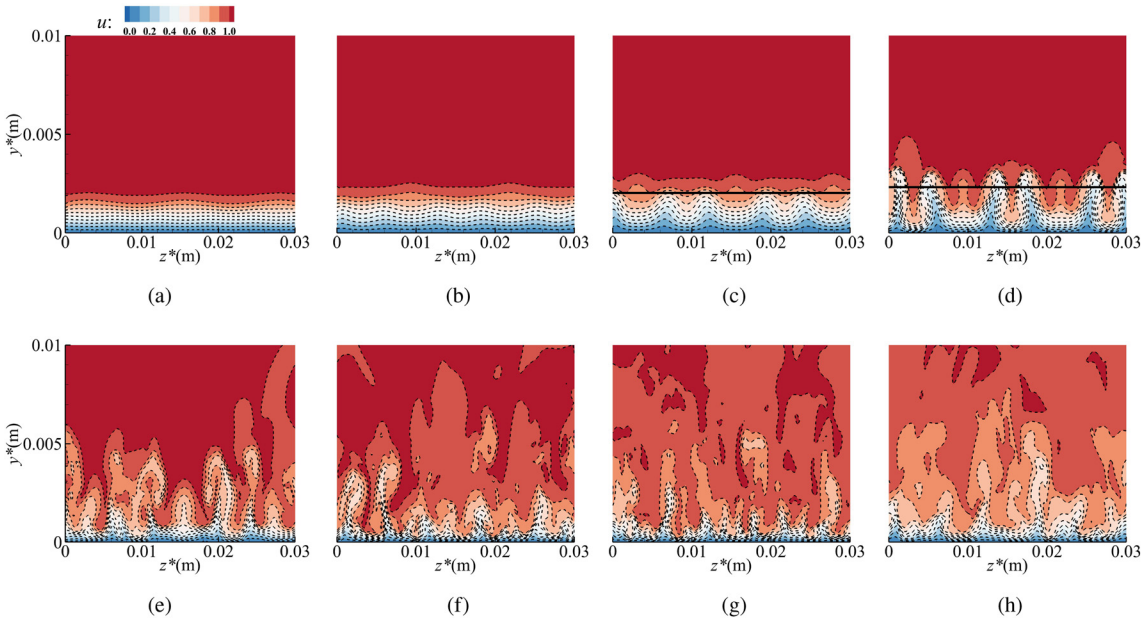

FIG. 3. Streamwise evolution of instantaneous streamwise velocity at (a) $x^* = 0.1$ m, (b) $x^* = 0.15$ m, (c) $x^* = 0.2$ m, (d) $x^* = 0.25$ m, (e) $x^* = 0.3$ m, (f) $x^* = 0.35$ m, (g) $x^* = 0.4$ m, and (h) $x^* = 0.6$ m. The horizontal solid line marks the location of the critical layer for mode (1, 1).

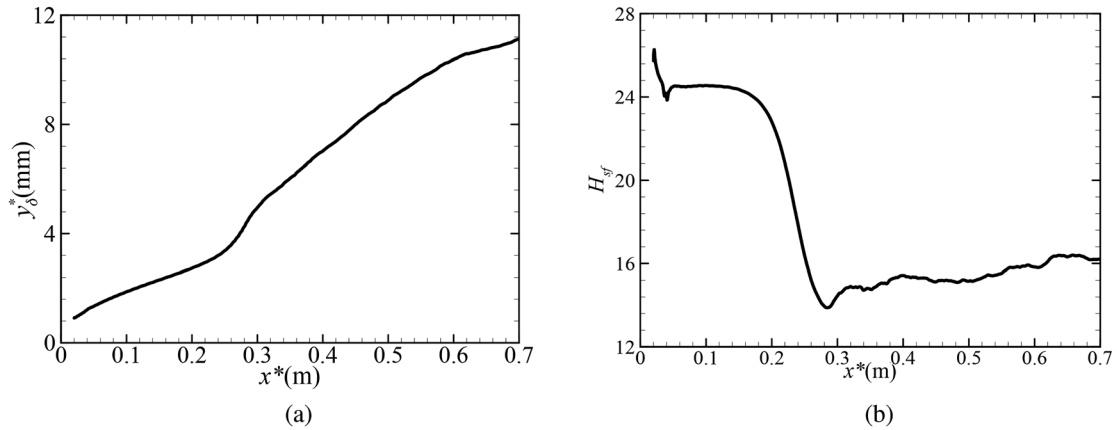

FIG. 5. Variation of (a) boundary layer integral thickness y^*_δ and (b) shape factor H_{sf} with streamwise location.

Although the time-averaged distribution is of principal interest for vehicle design, the highly unsteady property of the instantaneous heat flux may be troublesome when it is necessary to consider coupled thermal interaction with the solid surface. For example, transient heat conduction on the surface of hypersonic vehicles can significantly affect thermal stress and creep strain of the solid structure and in turn the lifetime of vehicles. Another severe problem that may cause catastrophical damage is thermal flutter. A recent experimental study by Daub *et al.*[53] found that a slight wall temperature difference in hypersonic boundary layer transition (within 10 K) resulted in occurrence of panel oscillations shortly after startup of the wind tunnel. The effect of transient flow fluctuations on the structural response has been further investigated.[54]

Since the flow is spanwise-homogeneous, spanwise averaging is performed in the general statistics. As a straightforward indicator of transition progress, Fig. 5 shows the development of the time- and spanwise-averaged nominal thickness y^*_δ and the shape factor H_{sf} of the boundary layer, where H_{sf} is the ratio of the displacement thickness and momentum thickness. The boundary layer transition is characterized by the rapid growth of boundary layer thickness and adjustment of the shape factor approximately in the region $0.2 < x^* < 0.35$ m.

Figure 6 shows the time- and spanwise-averaged averaged skin friction coefficient C_f, Stanton number St, and dimensional heat flux q^*_w. The Stanton number is defined by $St = q^*_w/[\rho^*_\infty u^*_\infty c^*_{p\infty}(T^*_{adb} - T^*_w)]$, where c_p is the specific heat at constant pressure. First, we examine whether the C_f or St curve eventually collapses onto the turbulent correlation. The displayed empirical C_f in the fully turbulent region is calculated by the van Driest II formula based on either Re_θ or Re_x,[15] where the difference is that the formula based on Re_x requires specification of the virtual leading edge (VLE) location. Without a unified theoretical foundation, this location is currently given by $x^*_{VLE} = 0$. The Stanton number is calculated by the Reynolds analogy in conjunction with the van Driest II formula based on Re_θ. The Reynolds analogy factor $2St/C_f$ was initially given by $Pr^{-2/3}$, as suggested by Colburn,[55] but a later high-speed experiment by Hopkins and Inouye[56] indicated a lower value. They found that the combination of the van Driest II and the analogy factor 1.0 could yield an accurate St via the Reynolds analogy in comparison with experimental data. Therefore, the Reynolds analogy factor is set to 1.0 in the present work.

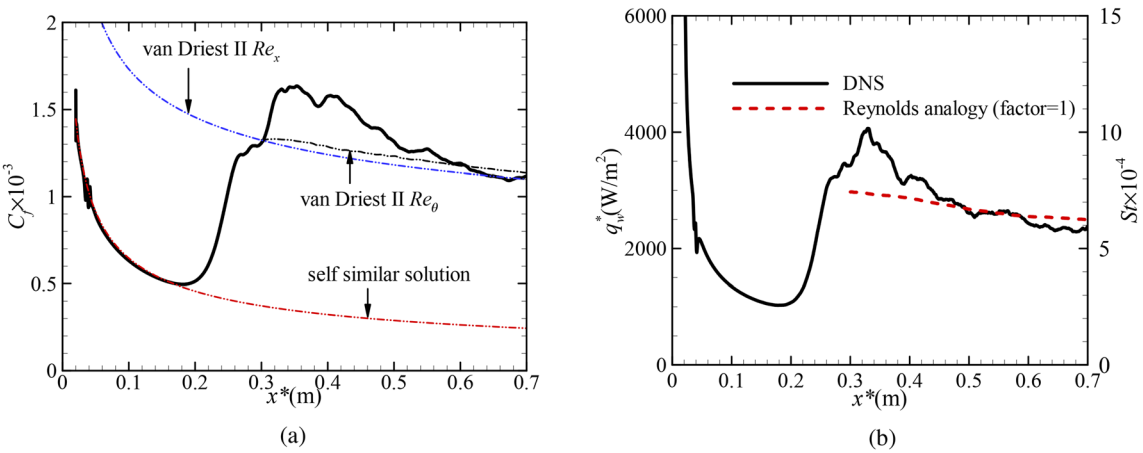

FIG. 6. Variation of (a) time- and spanwise-averaged skin friction and (b) heat flux and Stanton number with streamwise location.

With regard to the comparison between DNS results with theoretical or empirical formulas in Fig. 6, first, the C_f of the laminar boundary layer agrees well with that of the self-similar solution. The location where there is a deviation between the self-similar and DNS results for C_f, regarded as the transition location, is observed to be $x^* \approx 0.18$ m. In the transitional and fully turbulent regions, the averaged C_f and St generally collapse onto the empirical formulas for the turbulent region. In the transitional region, the C_f and St overshoot the turbulent correlations by at most around 23% and 38%, respectively.

To further investigate the fully developed turbulent region, the mean velocity profile is compared with the law of the wall. To remove the influence of mean density variations due to the effect of compressibility, the van Driest transformation for the mean velocity (which is mainly applicable at moderate or low Mach numbers) is utilized

$$U^+_{\mathrm{VD}} = \int_0^{\bar{u}^+} \sqrt{\frac{\bar{\rho}}{\bar{\rho}_w}}\, d\bar{u}^+(y). \tag{15}$$

Figure 7 compares the transformed mean velocity profile, the viscous sublayer law $u^+ = y^+$, and the incompressible log law $u^+ = 1/\kappa \ln(y^+) + 5.0$, where the von Kármán constant $\kappa \approx 0.4$. The mean velocity profile in the viscous sublayer and the log layer can be accordingly regarded as self-similar downstream of $x^* = 0.5$ m. There is agreement between the DNS data and the viscous sublayer law as well as the intercept of the log law. However, the slope of the transformed profile is slightly higher than $1/\kappa$. A similar observation can be made with regard to recent DNS results from the NASA Langley Center[57] at an approaching freestream Mach number 5.86 and identical freestream temperature and wall temperature. It can be inferred that the van Driest-transformed velocity profile may not agree with its incompressible counterpart if the Mach number is high or if wall cooling is involved. Nevertheless, it can be confirmed that the fully turbulent region reaches near self-similarity after $x^* = 0.5$ m can be confirmed.

C. Modal analysis

To quantify the modal growth, the maximum root mean square (r.m.s.) values of the streamwise velocity u'_{rms} of the leading modes $(0 \le m, n \le 3)$ are shown in Fig. 8. The results of linear parallel and nonparallel stability theories initiated at $x^* = 0.1$ m are also shown to enable identification of the linear instability stage. In the streamwise region $0.1 < x^* < 0.18$ m, the slopes of the curves for the DNS mode (1, 1) agree with those calculated by either LST or PSE. Extracted from the location $x^* = 0.175$ m, Fig. 9 shows a comparison of DNS and linear theories with respect to the u'_{rms} profile. Generally, both LST and PSE results agree with DNS data.

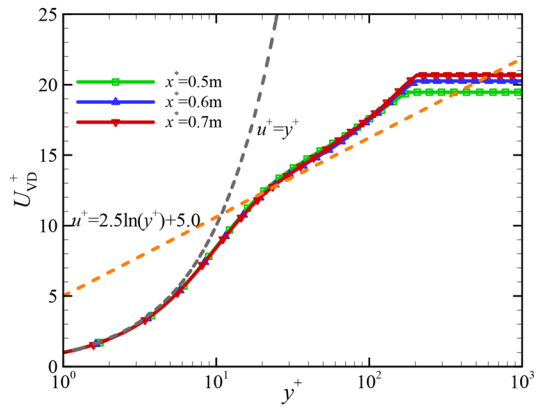

FIG. 7. The van Driest transformed mean velocity profile compared with the viscous sublayer law and the log law.

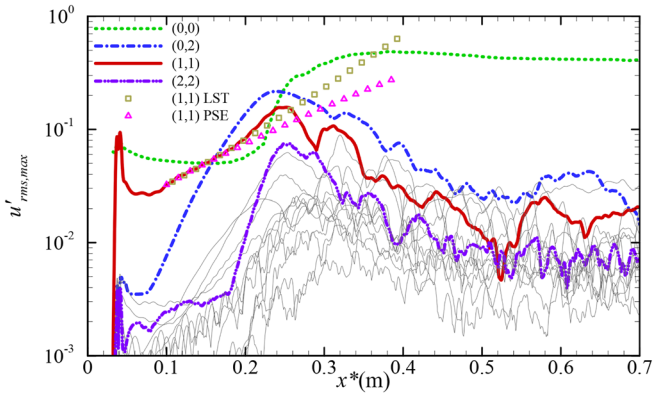

FIG. 8. Comparison of the maximum u'_{rms} between DNS and stability analyses. Gray lines represent the remaining unlabeled modes (m, n) $(0 \le m, n \le 3)$.

Downstream of the linear instability stage, the promotion and saturation of higher harmonics due to nonlinear wave interactions are recorded in Fig. 8. The magnitude of u'_{rms} indicates that the primary oblique mode (1, 1) and the streak mode (0, 2) are the most energetic in the transitional region, while other superharmonics like mode (2, 2) are weaker. Different from other superharmonics, mode (0, 2) is promoted appreciably in the early growth of instability waves owing to the sum interaction of the primary oblique waves. Significant growth of MFD is also observed to proceed from the transition location. It can be inferred that the pronounced MFD and the leading harmonics are probably responsible for the heat transfer on or approaching the wall. In Sec. IV, the contributions of MFD and the dominant harmonics will be analyzed.

IV. ANALYSIS OF ENERGY BUDGET AND MEAN FLOW PROFILE

The cause of the heat transfer overshoot can be revealed by analysis of the energy budget and the mean flow profile. The dimensional

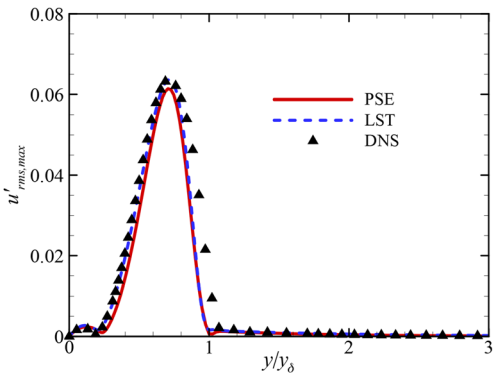

FIG. 9. Comparison of the maximum u'_{rms} profile between DNS and stability analyses at $x^* = 0.175$ m.

transport equation for the internal energy e per unit volume can be expressed as

$$\rho^*\left(\frac{\partial e^*}{\partial t^*}+\mathbf{V}^*\cdot\nabla e^*\right)=-\nabla\cdot\mathbf{q}^*-p^*\nabla\cdot\mathbf{V}^*+\Phi^*, \tag{16}$$

where $\mathbf{q}$ is the heat flux vector, and the term on the right-hand side represent thermal conduction, pressure dilatation, and viscous dissipation, respectively. After the time averaging operation, the unsteady time-dependent term in Eq. (16) is minor compared with the other terms. On the wall, with the advection term vanishing, the production terms on the right-hand side, including pressure dilatation and viscous dissipation, will be directly responsible for the considerable change in surface thermal conduction in the transitional region. Meanwhile, the rapid alteration in the flow state will significantly affect the nonzero advection term near but not on the wall. This advection effect in turn has a significant effect on the transport of momentum and energy, and this can be regarded as the root cause of the heat transfer overshoot. This argument provides the focal point for the energy analysis, namely, investigation of both the direct and root causes.

The significant terms in Eq. (16) can be decomposed into direct contributions from the mean flow field and higher-order moments arising from the effect of fluctuations, with the latter moments being further split into contributions from various harmonics. Specifically, the time- and spanwise-averaged viscous dissipation term is decomposed into contributions induced by shear and dilatation, denoted by Φ^*_ω and Φ_ϑ, respectively,[5]

$$\Phi^*=\Phi^*_\omega+\Phi^*_\vartheta, \tag{17}$$

where

$$\Phi^*_\omega=\langle\overline{\mu^*\omega^*_k\omega^*_k}\rangle,\quad \Phi^*_\vartheta=\langle\overline{\mu^*_d\vartheta^{*2}}\rangle,\quad \mu^*_d=\lambda^*+2\mu^* \tag{18}$$

with $\overline{(\cdot)}$ and $\langle\cdot\rangle$ denoting time and spanwise averaging, respectively. Here, in a Cartesian coordinate system, the vorticity components ω^*_k and the dilatation ϑ^* are expressed as

$$\omega^*_1=\frac{\partial w^*}{\partial y^*}-\frac{\partial v^*}{\partial z^*},\quad \omega^*_2=\frac{\partial u^*}{\partial z^*}-\frac{\partial w^*}{\partial x^*},\quad \omega^*_3=\frac{\partial v^*}{\partial x^*}-\frac{\partial u^*}{\partial y^*} \tag{19}$$

and

$$\vartheta^*=\frac{\partial u^*}{\partial x^*}+\frac{\partial v^*}{\partial y^*}+\frac{\partial w^*}{\partial z^*}. \tag{20}$$

Equation (18) demonstrates that the viscous dissipation induced by dilatation does not vanish even if Stokes' hypothesis holds, that is, $\lambda^*=-2\mu^*/3$. Considering the effects of fluctuation and spanwise distortion, we can decompose the shear-induced dissipation into four parts: $\Phi_\omega=\Phi_{\omega0}+\Phi_{\omega1}+\Phi_{\omega2}+\Phi_{\omega3}$. In this section, the instantaneous quantity is $\phi=\langle\bar\phi\rangle+\phi'$, with $\langle\bar\phi\rangle$ and ϕ' denoting the base flow superimposed by MFD and the disturbance excluding MFD, respectively. In this way, MFD is incorporated into the base flow to reflect the overall effect of the time- and spanwise-averaged field. The dimensionless expressions for $\Phi_{\omega0},\ldots,\Phi_{\omega3}$ are

$$\Phi_{\omega0}=\langle\bar\mu\rangle\langle\bar\omega_k\rangle\langle\bar\omega_k\rangle,\quad \Phi_{\omega1}=2\langle\bar\omega_k\rangle\langle\overline{\mu'\omega'_k}\rangle,\quad \Phi_{\omega2}=\langle\bar\mu\rangle\langle\overline{\omega'_k\omega'_k}\rangle,\quad \Phi_{\omega3}=\langle\overline{\mu'\omega'_k\omega'_k}\rangle, \tag{21}$$

where $\Phi_{\omega0}$, $\Phi_{\omega1}$, $\Phi_{\omega2}$, and $\Phi_{\omega3}$ reflect the effects of the time- and spanwise-averaged field, the second-order moment of the cross correlation between fluctuations in dynamic viscosity and vorticity, the second-order moment of the vorticity self-correlation, and the third-order moment, respectively. Both the streak mode (0, 2) and the primary mode (1, 1) contribute to the second- and third-order moment terms, while only the base flow and MFD determine the first term $\Phi_{\omega0}$.

Similarly, the dimensionless time- and spanwise-averaged dissipation induced by dilatation is written as $\Phi_\vartheta=\Phi_{\vartheta0}+\Phi_{\vartheta1}+\Phi_{\vartheta2}+\Phi_{\vartheta3}$, where

$$\Phi_{\vartheta0}=\langle\bar\mu\rangle\langle\bar\vartheta\rangle^2,\quad \Phi_{\vartheta1}=2\langle\bar\vartheta\rangle\langle\overline{\mu'\vartheta'}\rangle,\quad \Phi_{\vartheta2}=\langle\bar\mu\rangle\langle\overline{\vartheta'^2}\rangle,\quad \Phi_{\vartheta3}=\langle\overline{\mu'\vartheta'^2}\rangle. \tag{22}$$

The dimensionless time- and spanwise-averaged pressure dilatation term, denoted by T_p, is decomposed as $T_p=T_{p0}+T_{p1}$, where

$$T_{p0}=-\langle\bar p\rangle\left\langle\overline{\frac{\partial u_i}{\partial x_i}}\right\rangle,\quad T_{p1}=-\left\langle\overline{p'\frac{\partial u'_i}{\partial x_i}}\right\rangle. \tag{23}$$

The physical meanings of the decomposed terms of Φ_ϑ and T_p resemble those of Φ_ω. Sections IV A and IV B will analyze the terms that may be responsible for the overproduction of the internal energy. Moreover, the relative contributions of the leading harmonics to significant terms will be examined.

A. Surface energy budget

The budget of the internal energy on the wall surface reveals the direct cause of the rapidly varying thermal conduction term. Figure 10 shows the variation of the respective overall terms and their decomposed parts for pressure dilatation T_p, shear-induced dissipation Φ_ω, and dilatation-induced dissipation Φ_ϑ. Comparison of the dimensionless magnitudes shows that Φ_ω is significantly larger than Φ_ϑ and T_p in the transitional region, which is essentially different from what is known for the second mode, where the shear-induced dissipation is lower.[5] The main reason for these different findings is that the first and second modes possess the properties of vorticity and sound waves, respectively, which are associated with the mean shear and pressure, respectively.

Furthermore, comparison of the mean and fluctuating terms in Fig. 10 reveals the direct contribution of the mean field $\Phi_{\omega0}$ as a large portion of the total Φ_ω, while the sum of fluctuation-related parts $\Phi_{\omega1}+\Phi_{\omega2}+\Phi_{\omega3}$ is found to be less, although not negligible. Meanwhile, the Φ_ω part arising from the self-similar laminar base flow makes a minor contribution in the transitional region. Therefore, the pronounced $\Phi_{\omega0}$ is mainly attributable to the MFD. During the nonlinear interaction of the overall harmonics, the nonlinear production source term for MFD consists of interactions between every single mode and its complex conjugate, for example, $(1,1)+(-1,-1)\rightarrow(0,0)$. Owing to the symmetry of the Fourier space, the growth of MFD can be further ascribed to the growing amplitude of each mode. From this, we can infer that the dominant modes indirectly responsible for the gain in surface internal energy should be the most energetic modes (1, 1) and (0, 2). The overshoot of the amplitude of these dominant modes is important in generating the overshoot of aerodynamic heating. With regard to the fluctuation-induced terms, Fig. 10(b) confirms the significance of $\Phi_{\omega2}$, which indicates that the self-correlation

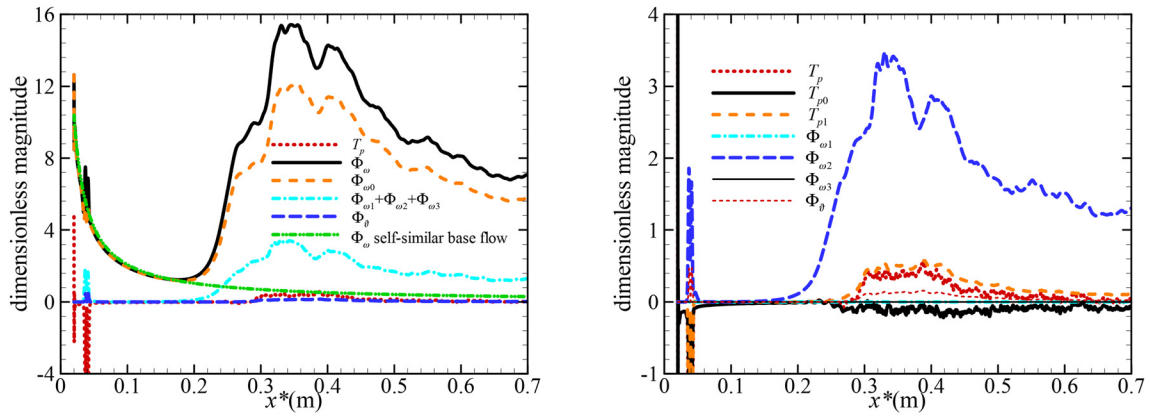

FIG. 10. Growth of terms in the internal energy transport equation on the wall (all non-dimensionalized by $\mu^*_\infty u^{*2}_\infty / l^2_{\text{ref}}$, where $l_{\text{ref}} = 1$ mm): (a) overall terms with high magnitude; (b) decomposed terms with low magnitude.

of the vorticity fluctuation ω'_k is greater than the cross correlation of ω'_k and μ'.

B. Advective heat transfer and mean flow profile

In the near-wall region, the nonzero advection term dominates the transport of the internal energy and the momentum, characterized by the wall-normal component of the Reynolds heat flux $-\overline{\rho v'' T''}$ and the Reynolds shear stress $-\overline{\rho v'' u''}$, respectively. Here, the fluctuation $(\cdot)''$ arising from the Favré density-weighted mean $\tilde{(\cdot)}$ is defined by $\phi'' = \phi - \tilde{\phi}$, where $\tilde{f} = \overline{\rho f}/\bar{\rho}$. Introducing the Favré averaging helps to take account of the compressibility effect and establish connections with transition modeling. Figure 11 shows the distributions of $-\langle\overline{\rho v'' T''}\rangle$ and $-\langle\overline{\rho v'' u''}\rangle$, which reveal visible enhancement in the transitional region, with their absolute maxima at $y/y_\delta = O(1/10)$. Thus, the transport of momentum and internal energy induced by advection in the transitional region is confirmed to overtake that in the fully developed turbulent region. Meanwhile, the enhanced region of $-\langle\overline{\rho v'' T''}\rangle$ appears to be broader than that of $-\langle\overline{\rho v'' u''}\rangle$. This finding corroborates the relative magnitudes of the observed overshoots of C_f and St, with maxima around 23% and 38%, respectively, where the heat flux overshoot is more obvious. Accompanying the overshoots of the Reynolds heat flux and shear stress in Fig. 11, the boundary layer thickness grows significantly.

Similar to the production terms on the right-hand side of Eq. (16), the wall-normal Reynolds heat flux can be decomposed into mean and fluctuating parts, with the latter being further decomposed into independent contributions of Fourier modes. The time- and spanwise-averaged term $R_T = \langle\overline{\rho v T}\rangle$ is decomposed as $R_T = R_{T0} + R_{T1} + R_{T2} + R_{T3} + R_{T4}$, where

$$R_{T0} = \langle\bar{\rho}\bar{v}\bar{T}\rangle, \quad R_{T1} = \langle\bar{\rho}\rangle\langle\overline{v'T'}\rangle, \quad R_{T2} = \langle\bar{T}\rangle\langle\overline{\rho'v'}\rangle, \\ R_{T3} = \langle\bar{v}\rangle\langle\overline{\rho'T'}\rangle, \quad R_{T4} = \langle\overline{\rho'v'T'}\rangle, \tag{24}$$

where R_{T0} characterizes the temperature transport via the wall-normal advection contributed by the self-similar base flow and MFD, $R_{T1} \sim R_{T3}$ represents the second-order moments, and R_{T4} represents the third-order moment. Owing to the orthogonality of different Fourier modes, the second-order moments $R_{T1} \sim R_{T3}$ arise solely from the self-correlation of each mode, with no contribution from the cross correlation. For example, the contribution of the primary mode (1, 1) to R_{T1} is given by

$$\langle\bar{\rho}\rangle\langle\overline{v'T'}\rangle_{(1,1)} = 4\bar{\rho}|\hat{v}|_{(1,1)}|\hat{T}|_{(1,1)}\cos\left(\Theta_{\hat{v}_{(1,1)}} - \Theta_{\hat{T}_{(1,1)}}\right), \tag{25}$$

where $|\hat{v}|$ and $|\hat{T}|$ are fluctuation amplitudes in Fourier space, Θ is the phase angle, and the constant coefficient 4 on the right-hand side arises from the quadrant symmetry property of mode (1, 1). Similar to the recent finding of Zhu *et al.*[58] that emphasizes the phase difference

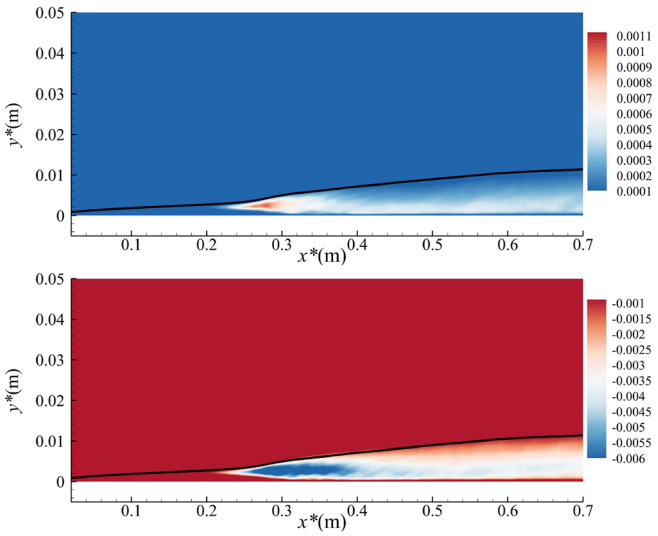

FIG. 11. Contours of the Reynolds shear stress $-\langle\overline{\rho v'' u''}\rangle$ (top) and the Reynolds heat flux $-\langle\overline{\rho v'' T''}\rangle$ (bottom) (non-dimensionalized by $\rho^*_\infty u^{*2}_\infty$ and $\rho^*_\infty u^*_\infty T^*_\infty$, respectively; the solid line indicates the location of the nominal boundary layer thickness).

in the dilatation term, for the aerothermal load reduction of hypersonic vehicles, Eq. (25) suggests that the phase difference between v' and T' is of particular significance.

Figure 11 illustrates that the enhanced Reynolds heat flux, as well as the strengthened vertical advective heat transfer, mainly appears in the outer region of the transitional boundary layer rather than in the very near-wall region. Therefore, the sources contributing to the advective heat transfer will be examined mainly in the outer boundary layer region $0.2 \leq y/y_\delta \leq 1$. Through the orthogonal decomposition in Eq. (25), it is straightforward to determine the relative contributions of the leading Fourier modes to a major second-order term of advective heat transfer, say, R_{T1}. Figure 12 shows the weight percent of modal contributions to R_{T1}, starting from the early linearly unstable stage ($x^* = 0.1$ m) to the downstream location of the mean heat flux peak ($x^* = 0.4$ m). At the location $x^* = 0.1$ m, Fig. 8 shows that the amplitude of the primary mode is at least one order of magnitude larger than the others. Accordingly, the contribution of mode (1, 1) to R_{T1} in Fig. 12(a) approaches 100% in the whole of outer boundary layer region $y/y_\delta > 0.6$. However, in the inner region, where the eigenfunction magnitude of mode (1, 1) falls rapidly, the contributions from other modes such as (0, 2) are comparable to that of the primary mode. Therefore, the dominant mode may not play an equally significant role in the energy budget right across the boundary layer.

Proceeding to $x^* = 0.2$ m where the nonlinear instability grows, we can see from Fig. 8 that the nonlinear difference interaction $(1,1) - (1,-1) \rightarrow (0,2)$ is much stronger than the self-sum interaction $(1,1) + (1,1) \rightarrow (2,2)$ in the early stage. Thus, it can be understood from Fig. 12(b) that the percentage contribution of the streak mode (0, 2) to R_{T1} increases considerably in the outer region $0.4 < y/y_\delta < 0.7$, while the contribution of mode $(2,2)$ remains tiny. Meanwhile, Fig. 8 illustrates that the r.m.s. amplitude of mode (1, 1) is overtaken by that of the streak mode (0, 2) at $x^* = 0.2$ m. Therefore, the region in which mode (1, 1) is dominant shrinks greatly in Fig. 12(b), where the intersection of the curves corresponding to modes (1, 1) and (0, 2) occurs at $y/y_\delta \approx 0.64$. However, the growth of mode (0, 2) encounters saturation at $x^* = 0.25$ m, while mode (1, 1) continues to grow, as shown by Fig. 8. Here, the dominant region of mode (1, 1) in Fig. 12(c) is enlarged compared with the location $x^* = 0.2$ m. Above a height $y/y_\delta \approx 0.52$ at $x^* = 0.25$ m, mode (1, 1) occupies over 50% of the overall contribution to R_{T1}. Recall from Fig. 11 that the peaks in the Reynolds shear stress and Reynolds heat flux are situated near the boundary layer edge for early instability stages rather than in the near-wall region for fully developed turbulence. Meanwhile, the magnitudes of the Reynolds shear stress and Reynolds heat flux have started to increase at the station $x^* = 0.25$ m, where the mean profiles of both the boundary layer and thermal boundary layer are changing. Therefore, the advection effect in the outer region is crucial to the overall internal energy transport, at least until the station $x^* = 0.25$ m, where the mean surface heat flux reaches 63% of the streamwise peak. The dominance of mode (1, 1) in the advection term of Eq. (16) continues, at least before saturation of all the harmonics.

Farther downstream at $x^* = 0.3$ m, where mode (2, 2) has grown and almost all modes saturate, Fig. 12(d) shows that the modal contributions to the advection term appear to be in a strongly competitive state. No major mode is observed that occupies over 50% of the contribution to R_{T1}, even for the streak mode near the wall. This is attributed to the fact that other superharmonics have been promoted and their accumulation is significant. Proceeding to the profiles $x^* = 0.35$ m and $x^* = 0.4$ m situated downstream of the heat flux peak, the streak mode (0, 2) is found to be the most important (over 30% of the entire

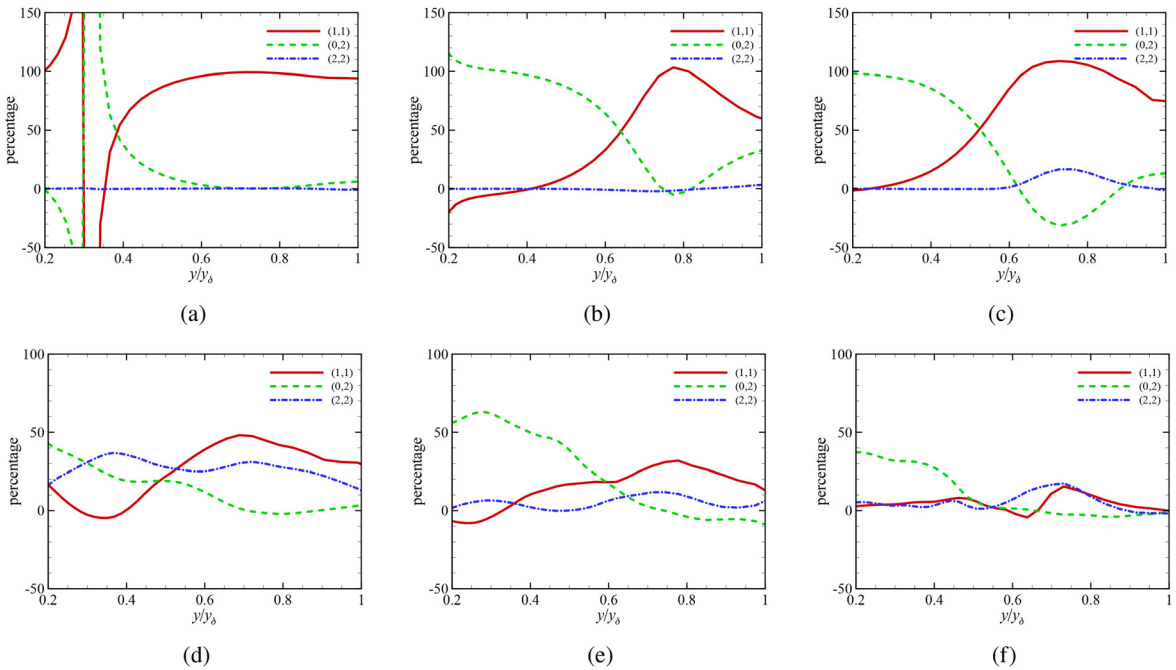

FIG. 12. Weight percent of modal contributions to the term R_{T1} at (a) $x^* = 0.1$ m, (b) $x^* = 0.2$ m, (c) $x^* = 0.25$ m, (d) $x^* = 0.3$ m, (e) $x^* = 0.35$ m, and (f) $x^* = 0.4$ m.

contribution) in the relatively inner region $y/y_\delta < 0.4$. In comparison, the weight of modes (1, 1) and (2, 2) decreases in the outer region, where none shows superiority over the rest. Generally, modes (1, 1) and (0, 2) are found to be dominant in the early outer and late near-wall regions, respectively. This conclusion agrees with Fig. 3 in that the modes with higher spanwise wavenumbers tend to originate from locations approaching the wall. With regard to the effect of heat transfer on the transition, the enhanced heat transfer further reshapes the mean temperature profile, which facilitates an interaction of MFD and other harmonics. Thus, the more rapid growth of harmonics are likely to occur before the saturation.

The analyses above highlight the main contributions to the R_{T1} term and to the Reynolds heat flux in the linear and nonlinear regimes. The strengthened Reynolds heat flux in the transitional region also affects both the mean flow profile and the mean heat flux significantly. Figure 13(a) shows the development of the dimensionless mean temperature profile from the linear unstable region to the fully developed turbulent region. The reference temperature and length scale for nondimensionalization are the freestream temperature and local boundary layer thickness, respectively. Considerable distortion of the mean temperature profile is observed in the outer boundary layer, starting from the rough transition location $x^* = 0.2$ m. Downstream of the streamwise mean heat flux peak location $x^* = 0.33$ m, denoted by $X_{St,\max}$, the mean temperature profile gradually becomes turbulent-like where the large temperature gradient moves downward to the near-wall region. The near-wall view of the temperature profile in Fig. 13(b) reveals that the maximum mean temperature is increased and the peak location gradually approaches the wall, starting from the laminar region to $X_{St,\max}$. Downstream of $X_{St,\max}$, the maximum mean temperature is attenuated. However, what does appear to be invariant downstream of the location of the peak heat flux is the dimensionless temperature gradient dT/dy at the wall. Figure 14(a) provides a clearer view of the wall temperature gradient, where dT/dy at the wall equals 17.27 at the location $X_{St,\max}$. The dimensionless wall temperature gradient reaches a near self-similar state downstream of $X_{St,\max}$. This seems sensible, since breakdown has occurred at the location $X_{St,\max}$ according to Figs. 2 and 3 and turbulent self-similarity is gradually established. The following quadrant analysis also provides evidence in Fig. 17 that at the location $x^* = 0.4$ m, the flow event performance is similar to that in the fully developed turbulent region, although the Stanton number has not yet collapsed onto the turbulent correlation.

It can be seen from Fig. 14(a) that the temperature gradient variation downstream of $X_{St,\max}$ is no longer directly attributable to the temperature profile reshaping contributed by the MFD. Although MFD continues to affect the dimensionless temperature peak $T_{\max}$ downstream of $X_{St,\max}$, little contribution from MFD to the dimensionless temperature gradient can be observed. Note that both the mean temperature and mean thermal conductivity are constant at the wall owing to the isothermal boundary condition. Therefore, the dimensionless Stanton number at the wall, characterizing the dimensionless heat flux, is not visibly affected by the nonlinear wave interactions downstream of $X_{St,\max}$. We can further infer that no heat transfer overshoot should appear if the mean boundary layer thickness downstream of $X_{St,\max}$ has the same growth rate as that of the fully turbulent region. This reasoning is based on the following relationship:

$$\frac{dT}{dy} = \frac{dT^*}{dy^*}\frac{y^*_\delta}{T^*_\infty}. \tag{26}$$

It can be seen that with a constant growth rate of the boundary layer thickness from $X_{St,\max}$ to the fully developed turbulent region, the dimensional temperature gradient at the wall is predicted to exhibit no substantial difference between the late transitional region and fully developed turbulent region. However, Fig. 14(b) shows a clear decrease in the dimensional temperature gradient at the wall downstream of $X_{St,\max}$. This observation and Eq. (26) demonstrate that the dimensional temperature gradient variation downstream of $X_{St,\max}$ is almost entirely attributable to the faster growth of the boundary layer thickness in the transitional region than the fully turbulent region. The faster growth in the transitional region is also shown by the statistical result in Fig. 5(a).

As further confirmation, a renormalized Stanton number is defined as $St_2 = St\, y^*_\delta/l^*_0$, which cancels the effect of the growth difference in the boundary layer thickness. Figure 15 shows that the transitional region downstream of $X_{St,\max}$ and the fully developed turbulent region share the same fitting slope of the $x^* \sim St_2$ correlation. Here, the start of the fully developed turbulent region is regarded as the

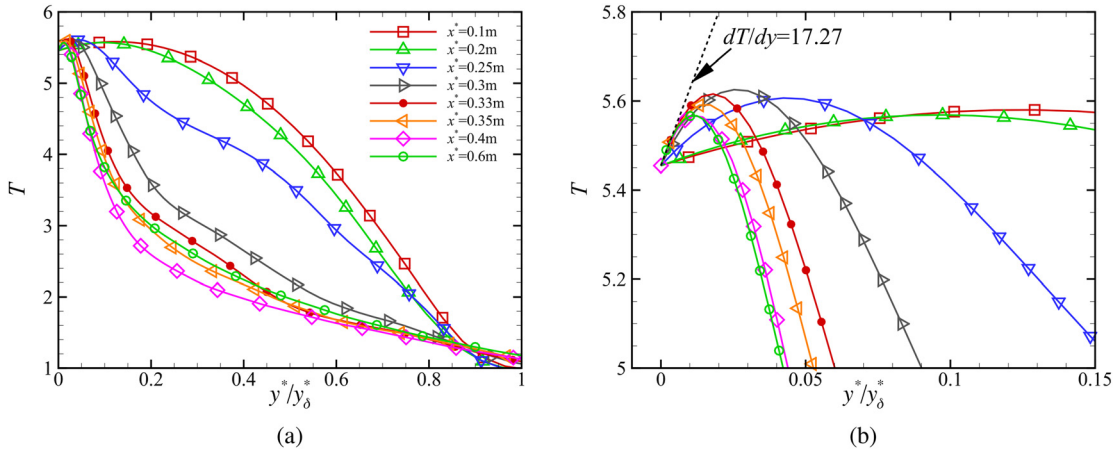

FIG. 13. Mean temperature profiles at different locations: (a) dimensionless profiles $y \sim T$; (b) profiles $y \sim T$ (near-wall region).

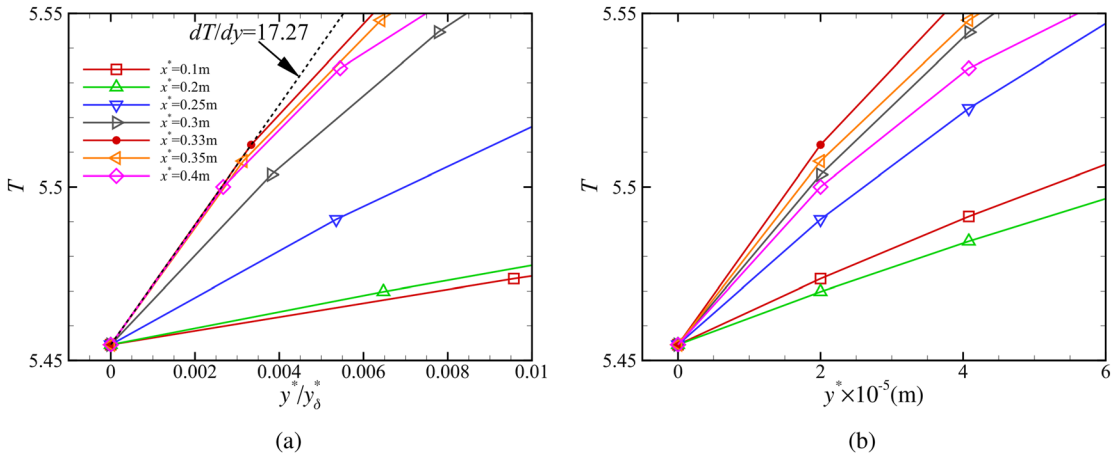

FIG. 14. Mean temperature profiles in the very near-wall region: (a) dimensionless profiles $y \sim T$; (b) dimensional profiles $y^* \sim T$.

location where the Stanton number St collapses onto the turbulent correlation. It is found that the late transitional region downstream of $X_{St,\max}$ is not essentially different from the fully turbulent region. No visible overshoot of the renormalized Stanton number is observed. Therefore, the new correlation $x^* \sim St_2$ indicates the possibility of similarity in the wall heat transfer behavior between the overshoot region and the fully developed turbulent region.

V. QUADRANT ANALYSIS

Quadrant analysis of the Reynolds shear stress clearly identifies the major flow events that are responsible for turbulence production. The four categories of flow events are Q1 ($u' > 0$, $v' > 0$, outward interaction), Q2 ($u' < 0$, $v' > 0$, ejection), Q3 ($u' < 0$, $v' < 0$, inward interaction), and Q4 ($u' > 0$, $v' < 0$, sweep), where Q2 and Q4 constitute the positive contribution to TKE production. By analogy with the quadrant analysis, scalar transport can be addressed in a similar manner, with the scalar transport events for the temperature

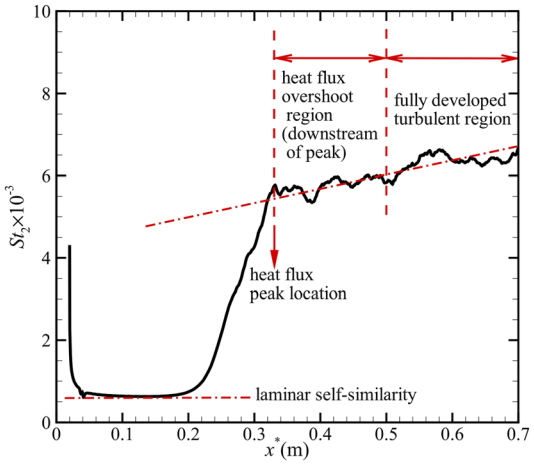

FIG. 15. Variation of renormalized Stanton number $St_2 = St\, y_\delta^*/l_0^*$ with streamwise location, where $l_0^* = 1$ mm.

consisting of Q1 ($T' > 0$, $v' > 0$, outward motion of hot fluid), Q2 ($T' < 0$, $v' > 0$, outward motion of cold fluid), Q3 ($T' < 0$, $v' < 0$, inward motion of cold fluid), and Q4 ($T' > 0$, $v' < 0$, inward motion of hot fluid). Octant analysis that incorporates the scalar T transport into the original quadrant analysis is an alternative approach, but the separate quadrant analyses of flow events and scalar transport events adopted here will help to identify the contributions to the Reynolds shear stress and Reynolds heat flux, respectively.

It should be noted that these flow events are generally more relevant to unsteady motion of fluids than to steady profile distortion. Consequently, steady disturbances, including MFD and stationary streak modes, are excluded from the total during the quadrant analysis, while the time-dependent fluctuation remains. These steady disturbances can be superimposed on the base flow, thereby generating a new distorted base flow. To avoid ambiguity, the time-dependent fluctuation is indicated by the subscript "flu" and is separated from the disturbance ϕ' in Eq. (7). In detail, decomposition of the instantaneous field ϕ is performed via

$$\phi = \phi_b + \phi'_{MFD} + \sum_{n>0} \phi'_{(0,n)} + \sum_{m,n} \phi'_{(m,n)}, \quad m > 0. \tag{27}$$

Combining the first two terms on the right-hand side of Eq. (27) yields

$$\phi = \langle \bar{\phi} \rangle + \sum_{n>0} \phi'_{(0,n)} + \phi'_{\mathrm{flu}}, \tag{28}$$

where the first two terms on the right-hand side constitute the new base flow. When the stationary waves $\phi'_{(0,n)}$ are excluded, the combined contribution of flow events to the heat flux term R_{T1} is expressed as $\langle \bar{\rho} \rangle \langle \overline{v'_{\mathrm{flu}} T'_{\mathrm{flu}}} \rangle$.

To record the flow events statistically, contours of the joint probability density functions (PDFs) for the fluctuations $u'_{\mathrm{flu}} \sim v'_{\mathrm{flu}}$ and $T'_{\mathrm{flu}} \sim v'_{\mathrm{flu}}$ are plotted in Fig. 16. The PDFs are normalized by the respective maxima, and the wall-normal height corresponds to the peak u'_{rms}. To show the evolution of the PDF, several profiles are extracted from different streamwise locations, namely, profile A

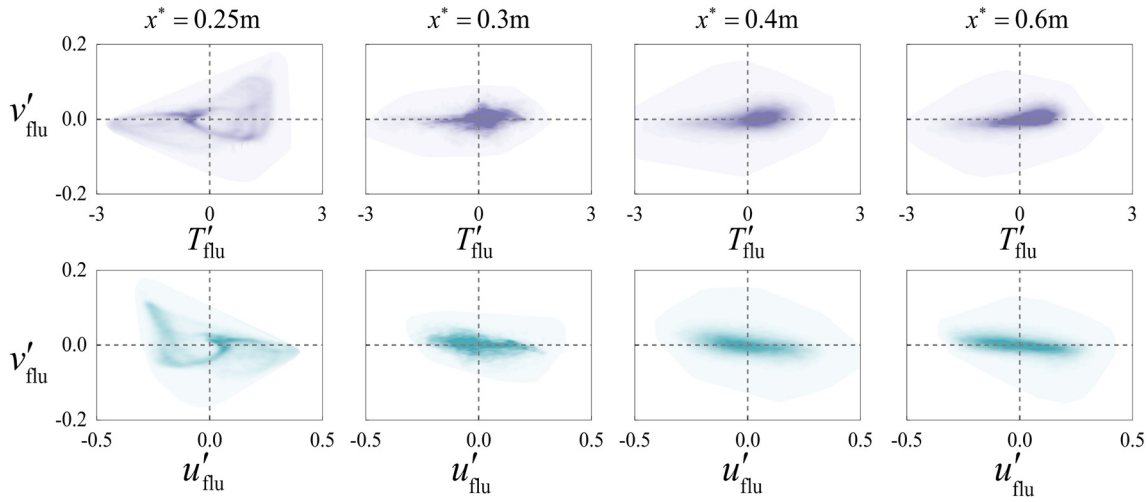

FIG. 16. Joint PDFs of the fluctuating velocities $u'_{flu} \sim v'_{flu}$ and fluctuations $T'_{flu} \sim v'_{flu}$ collected at the height of maximum u'_{rms}. The columns from left to right correspond to profiles A, B, C, and D, respectively.

($x^* = 0.25$ m, the rising stage of the $u'_{rms,max}$ of dominant modes), profile B ($x^* = 0.3$ m, the decreasing and rising stages of the modal $u'_{rms,max}$ and the mean Stanton number, respectively), profile C ($x^* = 0.4$ m, the decreasing stages of both modal $u'_{rms,max}$ and St), and profile D ($x^* = 0.6$ m, the fully developed turbulent region).

First, Fig. 16 highlights a unique feature of the rising stage of the fluctuation (profile A), namely, the relatively even distribution of the joint PDF over a wide range of fluctuation magnitude. By contrast, the joint PDFs of profiles B to D are narrowly concentrated near the origin (particularly for C and D, which are similar in shape). For profiles B to D, it is mainly the dark PDF region of the wall-normal v'_{flu} that shrinks. This indicates the cause of excessive production of the Reynolds stress in the transitional region from the perspective of fluid motions: a high probability of larger fluctuating velocities and temperature in the flow event.

Figure 16 shows a typical PDF performance selected from one wall-normal height. To provide a complete physical image across the boundary layer, the overall instantaneous data are treated statistically and recorded in the form of mean contributions in Fig. 17. As can be seen in Fig. 17(a), supporting the conclusion drawn from Fig. 16, the absolute contributions of events Q2 and Q4 to the Reynolds shear stress are considerably larger in early stages (profiles A and B) than in late stages (profiles C and D). The modal growths near profiles A and B, including those of higher harmonics, lead to enhancement of flow events. In comparison, the transitional profile C, approaching the fully developed turbulent region, exhibits an approximate balance between ejection and the sweep. This observation for profile C agrees with the conclusion for low-speed flow cases by Sayadi *et al.*[59] that the basic property of turbulent statistics is already established in the late stage after the skin friction overshoot.

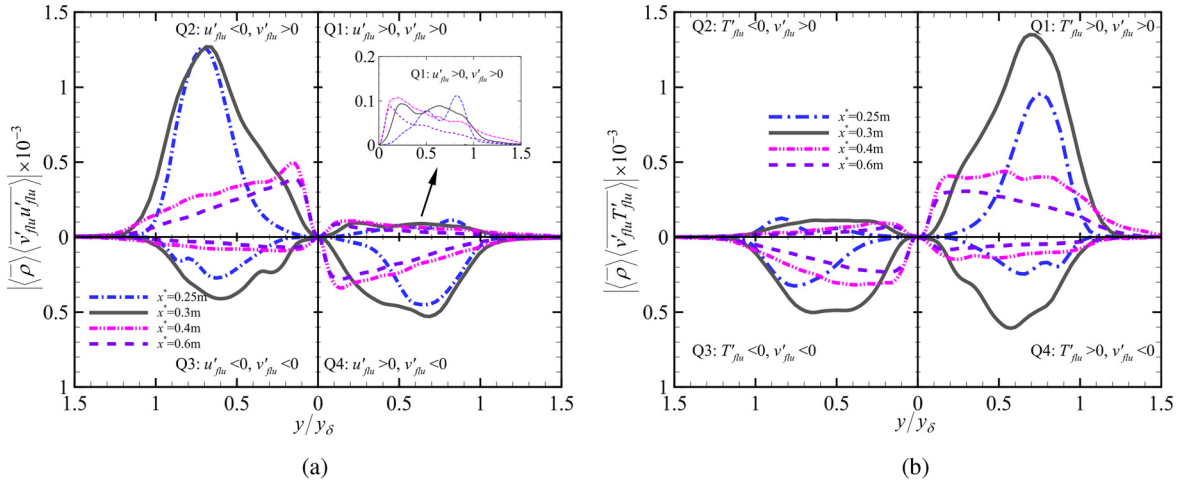

FIG. 17. Quadrant contributions to the (a) Reynolds shear stress $\langle\bar{\rho}\rangle\langle\overline{v'_{flu}u'_{flu}}\rangle$ and (b) heat flux $\langle\bar{\rho}\rangle\langle\overline{v'_{flu}T'_{flu}}\rangle$ from the flow events.

Furthermore, profiles A and B, not appearing in the late transitional stage, are essentially different from profiles C and D in terms of the position in the y direction of the peak contribution. For profiles A and B, the peak contribution of Q2 or Q4 is located in the outer boundary layer ($y/y_\delta \approx 0.7$), which is probably a result of the properties of the dominant instability wave. The reason for this inference is that the peak location of Q2 or Q4 coincides with the location of the greatest contribution of mode (1, 1) to R_{T1} in Figs. 12(c) and 12(d). In comparison, the peak locations of flow events near the fully developed turbulent region (profiles C and D) exhibit an inward shift to the inner boundary layer. For instance, for the fully turbulent profile D from Fig. 17(a), the peak locations for Q2 and Q4 coincide and move to $y/y_\delta \approx 0.143$, corresponding to $y^+ \approx 28.5$, which is at the bottom of the log layer approximately in the range $24 \leq y^+ \leq 70$. This observation demonstrates the transformation from instability (profiles A and B) to the turbulence (profile D) with respect to the contributions of flow events. The dominant scale of flow events varies from the large scale of instability waves to the near-wall small turbulent scale.

With regard to the Reynolds heat flux, Fig. 17(b) indicates that the scalar transport event Q1 ($T'_{\mathrm{flu}} \geq 0$, $v'_{\mathrm{flu}} \geq 0$) is the most significant in the transitional region, finally making a positive contribution to R_{T1}. In agreement with the explanation presented in Sec. IV B and resembling has been found recently by Zhu *et al.*[58] and Tian and Wen,[60] the small phase difference between the relevant fluctuations (v'_{flu} and T'_{flu} in our case) plays an important role in the instability process and aerothermal performance. The physical interpretation here is that the scalar transport event Q1 indicates that a positive v' corresponds to the equally positive T' carried by the coherent structure. Consequently, the low-temperature fluid is mainly advected approaching the wall. Thus, the rapid cooling in the outer boundary layer region reflected in Fig. 13(a) can be understood from the viewpoint of the quadrant analysis. There is also a clear similarity between the Reynolds shear stress and Reynolds heat flux profiles, which has also been reported for a fully developed turbulent boundary layer[61] but is less for the transitional flow. As indicated by the common behavior of the Reynolds shear stress and heat flux, hot ejection ($u'_{\mathrm{flu}} < 0$, $v'_{\mathrm{flu}} > 0$, $T'_{\mathrm{flu}} > 0$) should be dominant in the pretransitional and transitional regions, which agrees with the conclusion for incompressible cases by Volino and Simon.[39]

Another significant phenomenon is the imbalance between events Q2 and Q4 before breakdown, that is, profiles A and B. Ejection is more significant than sweep before the peak location of the skin friction and heat flux, while the two tend to achieve balance (although not exactly) in the fully turbulent region. Although ejection has already been found to be stronger than sweep in fully developed turbulence by Wallace,[38] it is still noteworthy here that ejection dominates sweep by a factor of more than two just upstream of the eventual oblique breakdown.

VI. CONCLUSIONS

In this paper, a pair of first-mode oblique waves with opposite wave angles have been introduced to initiate Mach 6 boundary layer transition via the wall blowing–suction technique. DNS, stability analyses, and a quadrant analysis have been utilized to reveal the mechanisms of oblique breakdown, as well as the overshoots of skin friction and heat transfer.

The instantaneous flow field identifies the formation and breakdown of outer staggered Λ-vortices near the critical layer and near-wall low-speed streaks. The time history also shows that the instantaneous heat flux can reach three to five times the average in the transitional region, which demonstrates a highly unsteady feature of heat transfer. By means of stability analyses and bi-Fourier transformation, the stages of localized receptivity, linear and nonlinear instabilities, modal saturation, and breakdown have been identified. The primary mode (1, 1) and streak mode (0, 2) are found to be the most energetic before breakdown.

A subsequent energy budget analysis indicates that the direct cause of the heat transfer overshoot is the enhanced shear-induced viscous dissipation at the wall. The viscous dissipation is further confirmed to be dominated by the direct contribution of the mean flow distortion. Furthermore, the fluctuation-related higher-order moments, particularly the self-correlation of the vorticity fluctuation, are smaller, but not negligible. During the rising stage of aerodynamic heating and before saturation of all the harmonics, the primary first mode accounts for a large proportion of the entire contribution to the advective heat transfer. In the vicinity of the location of the peak mean heat flux, the developed modes, including the primary oblique mode, streak mode, and a superharmonic (2, 2) mode across the boundary layer, compete with each other in contributing to the vertical advective heat exchange. The relative contributions of these modes to advective heat exchange are closely linked to the successive occurrence of fast growth and saturation of the leading harmonics induced by nonlinearity.

Examination of the mean temperature profile shows that the dimensionless temperature gradient varies little downstream of the location of the peak mean heat flux. The Stanton number St_2 renormalized by the local boundary layer thickness shows no difference between the transitional region downstream of the heat flux peak location and the fully developed turbulent region. This new correlation indicates the possibility of a similarity in wall heat transfer performance between the overshoot region and the fully turbulent region.

To interpret the source of the Reynolds stress and heat flux overproduction, a quadrant analysis has been performed. The flow event Q2 (ejection) considerably overtakes Q4 (sweep) in the transitional region, while the two nearly achieve balance in the fully developed turbulent region. Enhancement of both Q2 and Q4 is responsible for the overproduction of the Reynolds shear stress (and similarly for the Reynolds heat flux). This enhancement is mainly caused by the outer pronounced primary mode instability. Accordingly, the primary instability wave cannot be ignored in oblique breakdown, in addition to the well-known near-wall streak mode. In terms of the scalar transport event, the strong event ($T'_{\mathrm{flu}} > 0$, $v'_{\mathrm{flu}} > 0$) dominates the transitional region, which indicates notable downward transport of cold fluid. This explains why the outer mean temperature decreases rapidly in the transitional region.

ACKNOWLEDGMENTS

This research was supported by the National Natural Science Foundation of China through Grant No. 11872094, the National Defense Foundation Enhancement Program through Grant No. 2019JCJQJJ245, and the Research Grants Council, Hong Kong, under Contract No. 15216621.

AUTHOR DECLARATIONS

Conflict of Interest

The authors have no conflicts to disclose.

Author Contributions

Peixu Guo: Conceptualization (lead); Formal analysis (lead); Investigation (lead); Methodology (equal); Software (equal); Validation (lead); Writing – original draft (lead); Writing – review & editing (lead). **Fangcheng Shi:** Writing – review & editing (supporting). **Zhenxun Gao:** Funding acquisition (equal); Methodology (equal); Resources (lead); Software (equal); Supervision (equal); Writing – review & editing (supporting). **Chongwen Jiang:** Writing – review & editing (supporting). **Chun-Hian Lee:** Supervision (equal); Writing – review & editing (supporting). **Chih-Yung Wen:** Formal analysis (supporting); Funding acquisition (equal); Supervision (equal); Writing – original draft (supporting); Writing – review & editing (supporting).

DATA AVAILABILITY

The data that support the findings of this study are available from the corresponding author upon reasonable request.

APPENDIX: VALIDATION OF COMPUTER CODES

First, for the DNS code ACANS, a validation case in comparison with the results of Zhao *et al.*[62] is presented that simulates the mode S propagating in a Mach 6 2D flat-plate boundary layer. Table III shows the main computational setup. To excite the mode

TABLE III. Conditions for validation case of ACANS.

Ma_∞	T^*_∞ (K)	T^*_w (K)	Re_{unit} (m^{-1})	L_x (m)	L_y (m)	Grid points ($x \times y$)
6	43.18	293	1.05×10^7	0.2	0.04	1600×200

TABLE IV. Conditions for validation cases of CHASES.

Case	Ma_∞	T^*_∞ (K)	Re_{unit}	Re_0	ω/Re	β
C1	1.6	300	⋯	300	4×10^{-5}	0
C2	4.5	65.15	7.2×10^6	268.33	2.2×10^{-4}	0

S, a disturbance of the wall-normal mass flow rate is imposed on the wall between $x^*_1 = 0.01$ m and $x^*_2 = 0.015$ m, with the form $(\rho v)'_w = A_w \sin[2\pi(x^* - x^*_1)/(x^*_2 - x^*_1)] \sin(2\pi f^* t^*)$. The parameter setting for the disturbance follows that of Zhao *et al.*, namely, $A_w = 0.001$ and $f^* = 138.74$ kHz. The numerical methods are identical to those used in the investigation of the 3D cases in the present paper.

Figure 18(a) demonstrates favorable agreement between ACANS and the code of Zhao *et al.* in terms of the fluctuating pressure p'_{rms}. For further comparison, the nonparallel wavenumber for stability analyses is defined as

$$\sigma = \alpha - \mathrm{i}\frac{1}{\psi}\frac{d\psi}{dx}\bigg|_{y_r}, \tag{A1}$$

where the disturbance variable is $\psi = \hat{p}$ and the height is $y_r = 0$ (at the wall). The nonparallel growth rate is then given by the imaginary part σ_i. With regard to DNS data, the nonparallel growth rate is computed as

$$\sigma_i = \frac{1}{p'_{\text{rms}}}\frac{dp'_{\text{rms}}}{dx}, \tag{A2}$$

where x^* is non-dimensionalized by the reference length scale $l_{\text{ref}} = \sqrt{\mu^*_\infty x^*/\rho^*_\infty u^*_\infty}$. Figure 18(b) shows good agreement of σ_i between the present DNS, the present LST, and the LST of Zhao *et al.* in the range of $0.08 \le x^* \le 0.12$ m, where stable modes such as entropy and vorticity modes decay and linear instability dominates. In the region $x^* > 0.12$ m, better agreement is reached between DNS and PSE, where the nonparallel effect seems to be

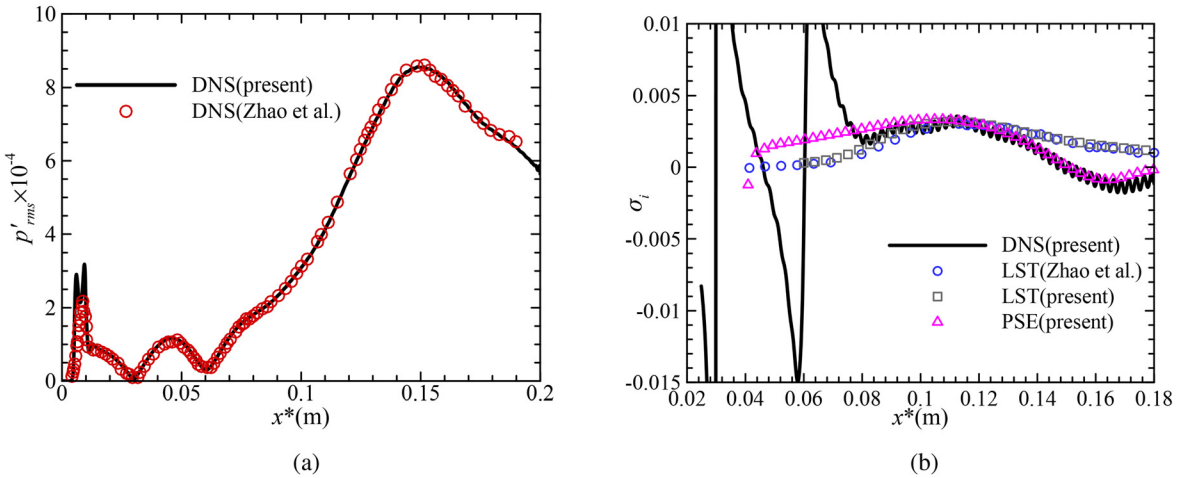

FIG. 18. Comparisons of (a) the fluctuating pressure amplitude and (b) the nonparallel growth rate between ACANS, CHASES, and codes in the literature.

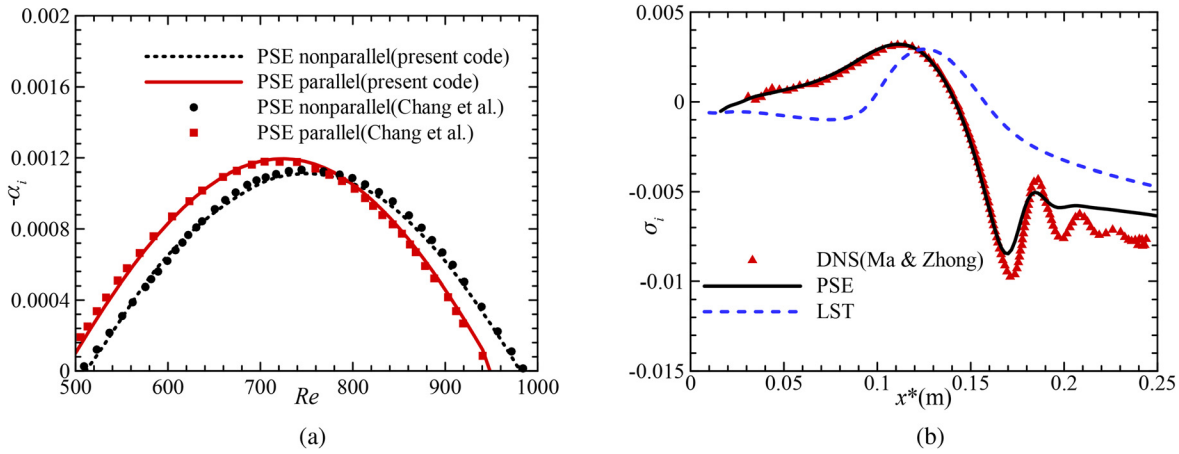

FIG. 19. Comparisons of the parallel and nonparallel growth rates between CHASES and codes in the literature(a) case C1; (b) case C2.

significant. Generally, ACANS is proved to simulate the development of the instability mode in the hypersonic boundary layer accurately.

Since the present LST code has been validated previously,[48,49] the next cases C1 and C2 are used to examine the PSE module of CHASES, and these are compared with the PSE cases of Chang *et al.*[63] and the DNS cases of Ma and Zhong.[64] Both cases C1 and C2 simulate the instability mode of a flat-plate boundary layer. The parameter conditions are given in Table IV. The base flow is given by the self-similar solution with adiabatic wall condition. The reference length scale is $l_{\mathrm{ref}} = \sqrt{\mu^*_\infty x^*_0/\rho^*_\infty u^*_\infty}$, on which the Reynolds number Re_0 is based. Figure 19 displays the results for $-\alpha_i$ for case C1 and σ_i for case C2. Good agreement is observed in terms of the PSE results between CHASES and the codes in the literature for case C1. In addition, the results for case C2 reveal better agreement between the PSE and DNS of Ma and Zhong than between LST and DNS. Thus, finally, the reliability of CHASES is verified.

REFERENCES

[1]L. M. Mack, "Linear stability theory and the problem of supersonic boundary-layer transition," AIAA J. **13**, 278–289 (1975).
[2]L. M. Mack, "Boundary-layer linear stability theory," Technical Report No. 709 (California Institute of Technology, Pasadena Jet Propulsion Laboratory, 1984).
[3]W. S. Saric, H. L. Reed, and E. J. Kerschen, "Boundary-layer receptivity to free-stream disturbances," Annu. Rev. Fluid Mech. **34**, 291–319 (2002).
[4]A. Novikov, I. Egorov, and A. Fedorov, "Direct numerical simulation of wave packets in hypersonic compression-corner flow," AIAA J. **54**, 2034–2050 (2016).
[5]Y. Zhu, C. Zhang, X. Chen, H. Yuan, J. Wu, S. Chen, C. Lee, and M. Gad-el Hak, "Transition in hypersonic boundary layers: Role of dilatational waves," AIAA J. **54**, 3039–3049 (2016).
[6]Y. Zhu, X. Chen, J. Wu, S. Chen, C. Lee, and M. Gad-el Hak, "Aerodynamic heating in transitional hypersonic boundary layers: Role of second-mode instability," Phys. Fluids **30**, 011701 (2018).
[7]X. Chen, Y. Zhu, and C. Lee, "Interactions between second mode and low-frequency waves in a hypersonic boundary layer," J. Fluid Mech. **820**, 693–735 (2017).
[8]M. Goldstein, "The evolution of Tollmien-Schlichting waves near a leading edge," J. Fluid Mech. **127**, 59–81 (1983).
[9]M. E. Goldstein, "Scattering of acoustic waves into Tollmien-Schlichting waves by small streamwise variations in surface geometry," J. Fluid Mech. **154**, 509–529 (1985).
[10]A. Fedorov, A. Ryzhov, V. Soudakov, and S. Utyuzhnikov, "Receptivity of a high-speed boundary layer to temperature spottiness," J. Fluid Mech. **722**, 533–553 (2013).
[11]P. Balakumar and M. A. Kegerise, "Receptivity of hypersonic boundary layers over straight and flared cones," AIAA J. **53**, 2097–2109 (2015).
[12]H. Goparaju and D. Gaitonde, "Receptivity and instability of entropy-layer disturbances in blunted plate transition," AIAA Paper No. 2021-2877, 2021.
[13]J. Zhou and W. Cao, "Effects of entropy layer on the boundary layer over hypersonic blunt cones considering entropy swallowing," Phys. Fluids **33**, 076101 (2021).
[14]H. Raposo, S. Mughal, and R. Ashworth, "Acoustic receptivity and transition modeling of Tollmien-Schlichting disturbances induced by distributed surface roughness," Phys. Fluids **30**, 044105 (2018).
[15]K. J. Franko and S. K. Lele, "Breakdown mechanisms and heat transfer overshoot in hypersonic zero pressure gradient boundary layers," J. Fluid Mech. **730**, 491–532 (2013).
[16]C. Lee and X. Jiang, "Flow structures in transitional and turbulent boundary layers," Phys. Fluids **31**, 111301 (2019).
[17]J. Sivasubramanian and H. F. Fasel, "Numerical investigation of the development of three-dimensional wavepackets in a sharp cone boundary layer at Mach 6," J. Fluid Mech. **756**, 600–649 (2014).
[18]W. Eißler and H. Bestek, "Spatial numerical simulations of linear and weakly nonlinear wave instabilities in supersonic boundary layers," Theor. Comput. Fluid Dyn. **8**, 219–235 (1996).
[19]I. V. Egorov and A. V. Novikov, "Direct numerical simulation of laminar-turbulent flow over a flat plate at hypersonic flow speeds," Comput. Math. Math. Phys. **56**, 1048–1064 (2016).
[20]J. Sivasubramanian and H. F. Fasel, "Direct numerical simulation of transition in a sharp cone boundary layer at Mach 6: Fundamental breakdown," J. Fluid Mech. **768**, 175–218 (2015).
[21]C. Hader and H. F. Fasel, "Direct numerical simulations of hypersonic boundary-layer transition for a flared cone: Fundamental breakdown," J. Fluid Mech. **869**, 341–384 (2019).
[22]S. Unnikrishnan and D. V. Gaitonde, "First-mode-induced nonlinear breakdown in a hypersonic boundary layer," Comput. Fluids **191**, 104249 (2019).
[23]S. Unnikrishnan and D. V. Gaitonde, "Linear, nonlinear and transitional regimes of second-mode instability," J. Fluid Mech. **905**, A25 (2020).
[24]H. Fasel, A. Thumm, and H. Bestek, "Direct numerical simulation of transition in supersonic boundary layers: Oblique breakdown," in *Proceedings of the Fluids Engineering Conference* (ASME, 1993), pp. 77–92.
[25]C. D. Pruett and C.-L. Chang, "Spatial direct numerical simulation of high-speed boundary-layer flows. II. Transition on a cone in Mach 8 flow," Theor. Comput. Fluid Dyn. **7**, 397–424 (1995).

[26]C. Mayer, S. Wernz, and H. Fasel, "Investigation of oblique breakdown in a supersonic boundary layer at Mach 2 using DNS," AIAA Paper No. 2007-949, 2007.
[27]C. S. Mayer, D. A. Von Terzi, and H. F. Fasel, "Direct numerical simulation of complete transition to turbulence via oblique breakdown at Mach 3," J. Fluid Mech. **674**, 5–42 (2011).
[28]A. B. Hartman, C. Hader, and H. F. Fasel, "Nonlinear transition mechanism on a blunt cone at Mach 6: Oblique breakdown," J. Fluid Mech. **915**, R2 (2021).
[29]A. C. Laible and H. F. Fasel, "Continuously forced transient growth in oblique breakdown for supersonic boundary layers," J. Fluid Mech. **804**, 323–350 (2016).
[30]A. Fezer and M. Kloker, "DNS of transition mechanisms at Mach 6.8–flat plate vs. sharp cone," in *Proceedings of the* West East High Speed Flow Fields (CIMNE, Barcelona, Spain, 2002), pp. 434–441.
[31]P. Wassermann and M. Kloker, "Mechanisms and passive control of crossflow-vortex-induced transition in a three-dimensional boundary layer," J. Fluid Mech. **456**, 49–84 (2002).
[32]S. Sharma, M. S. Shadloo, A. Hadjadj, and M. J. Kloker, "Control of oblique-type breakdown in a supersonic boundary layer employing streaks," J. Fluid Mech. **873**, 1072–1089 (2019).
[33]M. S. Holden, "An experimental investigation of turbulent boundary layers at high Mach number," Technical Report No. 111242 (Cornell Aeronautical Laboratory, 1972).
[34]T. Horvath, S. Berry, B. Hollis, B. Singer, and C.-L. Chang, "Boundary layer transition on slender cones in conventional and low disturbance Mach 6 wind tunnels," AIAA Paper No. 2002-2743, 2002.
[35]T. Wadhams, E. Mundy, M. MacLean, and M. Holden, "Ground test studies of the HIFiRE-1 transition experiment. I. Experimental results," J. Spacecr. Rockets **45**, 1134–1148 (2008).
[36]L. Brandt and D. S. Henningson, "Transition of streamwise streaks in zero-pressure-gradient boundary layers," J. Fluid Mech. **472**, 229–261 (2002).
[37]W. Willmarth and S. Lu, "Structure of the Reynolds stress near the wall," J. Fluid Mech. **55**, 65–92 (1972).
[38]J. M. Wallace, "Quadrant analysis in turbulence research: History and evolution," Annu. Rev. Fluid Mech. **48**, 131–158 (2016).
[39]R. J. Volino and T. W. Simon, "An application of octant analysis to turbulent and transitional flow data," J. Turbomach. **116**, 752–758 (1994).
[40]K. Nolan, E. Walsh, and D. McEligot, "Quadrant analysis of a transitional boundary layer subject to free-stream turbulence," J. Fluid Mech. **658**, 310–335 (2010).
[41]K. P. Nolan and T. A. Zaki, "Conditional sampling of transitional boundary layers in pressure gradients," J. Fluid Mech. **728**, 306–339 (2013).
[42]G. I. Park, J. M. Wallace, X. Wu, and P. Moin, "Boundary layer turbulence in transitional and developed states," Phys. Fluids **24**, 035105 (2012).
[43]J. D. Anderson, *Computational Fluid Dynamics: The Basics with Applications* (McGraw-Hill, 1995).
[44]F. Bertolotti, "Linear and nonlinear stability of boundary layer with streamwise varying properties," Ph.D. thesis (Ohio State University, 1991).
[45]C.-L. Chang and M. R. Malik, "Oblique-mode breakdown and secondary instability in supersonic boundary layers," J. Fluid Mech. **273**, 323–360 (1994).
[46]Y. Vigneron, J. Tannehill, and J. Rakich, "Calculation of supersonic viscous flow over delta wings with sharp subsonic leading edges," AIAA Paper No. 1978-1137, 1978.
[47]M. R. Malik, "Numerical methods for hypersonic boundary layer stability," J. Comput. Phys. **86**, 376–413 (1990).
[48]P. Guo, Z. Gao, C. Jiang, and C. Lee, "Linear stability analysis on the most unstable frequencies of supersonic flat-plate boundary layers," Comput. Fluids **197**, 104394 (2020).
[49]P. Guo, Z. Gao, C. Jiang, and C. Lee, "Sensitivity analysis on supersonic-boundary-layer stability subject to perturbation of flow parameters," Phys. Fluids **33**, 084111 (2021).
[50]X. Huai, R. D. Joslin, and U. Piomelli, "Large-eddy simulation of transition to turbulence in boundary layers," Theor. Comput. Fluid Dyn. **9**, 149–163 (1997).
[51]Y. Xue, L. Wang, Z. Wang, and S. Fu, "Gap-induced transition via oblique breakdown at Mach 6," Shock Waves **29**, 1181–1190 (2019).
[52]S. J. Kline, W. C. Reynolds, F. Schraub, and P. Runstadler, "The structure of turbulent boundary layers," J. Fluid Mech. **30**, 741–773 (1967).
[53]D. Daub, S. Willems, and A. Gülhan, "Experiments on aerothermoelastic fluid-structure interaction in hypersonic flow," J. Sound Vib. **531**, 116714 (2022).
[54]D. Huang, "Development of a hypersonic aerothermoelastic framework and its application to flutter and aerothermoelastic scaling of skin panels," Ph.D. thesis (University of Michigan, 2019).
[55]A. P. Colburn, "A method of correlating forced convection heat-transfer data and a comparison with fluid friction," Int. J. Heat Mass Transfer **7**, 1359–1384 (1964).
[56]E. J. Hopkins and M. Inouye, "An evaluation of theories for predicting turbulent skin friction and heat transfer on flat plates at supersonic and hypersonic Mach numbers," AIAA J. **9**, 993–1003 (1971).
[57]C. Zhang, L. Duan, and M. M. Choudhari, "Direct numerical simulation database for supersonic and hypersonic turbulent boundary layers," AIAA J. **56**, 4297–4311 (2018).
[58]Y. Zhu, D. Gu, W. Zhu, S. Chen, C. Lee, and E. S. Oran, "Dilatational-wave-induced aerodynamic cooling in transitional hypersonic boundary layers," J. Fluid Mech. **911**, A36 (2021).
[59]T. Sayadi, C. W. Hamman, and P. Moin, "Direct numerical simulation of complete H-type and K-type transitions with implications for the dynamics of turbulent boundary layers," J. Fluid Mech. **724**, 480–509 (2013).
[60]X. Tian and C. Wen, "Growth mechanisms of second-mode instability in hypersonic boundary layers," J. Fluid Mech. **908**, R4 (2021).
[61]H. Kong, H. Choi, and J. S. Lee, "Direct numerical simulation of turbulent thermal boundary layers," Phys. Fluids **12**, 2555–2568 (2000).
[62]R. Zhao, C. Wen, X. Tian, T. Long, and W. Yuan, "Numerical simulation of local wall heating and cooling effect on the stability of a hypersonic boundary layer," Int. J. Heat Mass Transfer **121**, 986–998 (2018).
[63]C.-L. Chang, M. R. Malik, G. Erlebacher, and M. Y. Hussaini, "Linear and nonlinear PSE for compressible boundary layers," Technical Report No. 191537 (NASA, 1993).
[64]Y. Ma and X. Zhong, "Receptivity of a supersonic boundary layer over a flat plate. I. Wave structures and interactions," J. Fluid Mech. **488**, 31–78 (2003).